Reactive control of isolated unsteady streaks in a laminar boundary layer

Kyle M. Bade[1], Ronald E. Hanson[2], Brandt A. Belson[3], Ahmed M. Naguib[1],†, Philippe Lavoie[2] and Clarence W. Rowley[3]

[1]Department of Mechanical Engineering, Michigan State University, East Lansing, MI 48823, USA

[2]Institute for Aerospace Studies, University of Toronto, Toronto, Ontario M3H 5T6, Canada

[3]Department of Mechanical and Aerospace Engineering, Princeton University, Princeton, NJ 08544, USA

This study is motivated by controlling transient growth and subsequent bypass transition of the laminar boundary layer to turbulence. In experiments employing a model problem, an active roughness element is used to introduce steady/unsteady streak disturbances in a Blasius boundary layer. This tractable arrangement enables a systematic investigation of the evolution of the disturbances and of potential methods to control them in real time. The control strategy utilizes wall-shear-stress sensors, upstream and downstream of a plasma actuator, as inputs to a model-based controller. The controller is designed using empirical input/output data to determine the parameters of simple models, approximating the boundary layer dynamics. The models are used to tune feedforward and feedback controllers. The control effect is examined over a range of roughness-element heights, free stream velocities, feedback sensor positions, unsteady disturbance frequencies and control strategies; and is found to nearly completely cancel the steady-state disturbance at the downstream sensor location. The control of unsteady disturbances exhibits a limited bandwidth of less than 1.3 Hz. However, concurrent modelling demonstrates that substantially higher bandwidth is achievable by improving the feedforward controller and/or optimizing the feedback sensor location. Moreover, the model analysis shows that the difference in the convective time delay of the roughness- and actuator-induced disturbances over the control domain must be known with high accuracy for effective feedforward control. This poses a limitation for control effectiveness in a stochastic environment, such as in bypass transition beneath a turbulent free stream; nonetheless, feedback can remedy some of this limitation.

Key words: boundary layer control, flow control, instability control

1. Introduction

Bypass boundary layer transition is initiated by the formation and growth of streamwise-elongated disturbances known as streaks (for reviews of bypass transition, see Reshotko (2001), Zaki & Durbin (2005), Durbin & Wu (2007) and Zaki (2013)).

† Email address for correspondence: naguib@egr.msu.edu

Thus, active sensing and control of streaks within their growth region could allow the delay or prevention of bypass transition and turbulence. To understand the basis for such control efforts, a brief account of the physics of streaks in bypass transition is first provided. The initiation of streaks within the boundary layer was found in Zaki & Durbin (2005) to result from resonant interaction between the Orr–Sommerfeld and Squire modes, which favours the formation of low-frequency (streamwise elongated) disturbances. Once initiated, the streaks exhibit linear transient growth associated with algebraic increase of their energy in the streamwise direction (Matsubara & Alfredsson 2001). Physically, the formation and growth of the streaks may be explained via Landahl's 'lift-up' mechanism (Landhal 1980), where wall-normal velocity disturbances cause the movement of fluid across the boundary layer shear. As a result, low-speed fluid is translated away from the wall while high-speed fluid is pushed towards the wall, creating quasi-periodic low- and high-speed streaks side-by-side along the spanwise direction. Once the streamwise-velocity disturbance produced by the streaks ('streak amplitude') grows to a certain level, the streaks themselves may become unstable, leading to the formation of turbulent spots. Early studies of this secondary instability include Andersson *et al.* (2001) and Asai, Minagawa & Nishioka (2002) who examined varicose and sinuous instability modes of the streaks. Both of these studies focused on the instability of steady streaks; however, in actual bypass transition, streaks are unsteady. The effect of unsteadiness on streak instability was examined by Vaughan & Zaki (2011), where it was shown that unsteady streaks are more unstable than steady ones, and that the critical streak amplitude for instability is 8.5 % (substantially lower than the 26 % found for steady streaks (Andersson *et al.* 2001)).

The reactive control strategy examined in the current work is designed to target streaks during the early stage of linear growth, well ahead of reaching critical streak amplitude. This enables the introduction of counter-disturbances that will superpose linearly with the streak disturbances to weaken the streaks and prevent them from reaching critical amplitudes. Therefore, the streaks examined in this study possess amplitudes well below critical magnitude. Furthermore, the control strategy is applied to unsteady streaks, given the importance of streak unsteadiness, as mentioned above. It is also noteworthy that the present control strategy targets all streaks regardless of whether they eventually become unstable and develop turbulent spots or remain benign (Nolan & Zaki 2013). The selective control of only unstable streaks, though would increase the control efficiency of the system, it would require accurate estimation of the velocity field within a cross-flow plane and application of bi-global stability analysis (similar to that done by Vaughan & Zaki (2011)) on this field in real time to identify the unstable streaks. This is expected to slow down the control system substantially.

Experimental demonstrations of streak disturbance control are rare. Jacobson & Reynolds (1998) conducted an experimental demonstration of steady streak disturbance control in a laminar boundary layer using oscillating cantilever-beam synthetic jets, which introduced a pair of counter-rotating vortices, opposite in sign to that generated by an upstream cylindrical element (protruding outside the boundary layer). An *ad hoc* linear feedback controller was then used to target dynamic disturbances that were introduced using suction and the results demonstrated these disturbances could indeed be reduced in magnitude.

In one of the more successful studies, Lundell (2007) used suction/blowing at the wall, coupled with wall-shear-stress sensing and feedforward control to delay flow instability of streaks induced by free stream turbulence. While this work constituted an

instructive demonstration of successful bypass boundary layer transition delay, Lundell tuned the level of flow control manually. This leads to the focus of the current control efforts which aim to prevent, or delay, streak disturbance instability and boundary layer breakdown to turbulence through the development and implementation of a model-based feedforward and feedback control system to actively sense streaks and apply appropriate flow forcing, to weaken or eliminate these streaks in real time.

Following the work of Jacobson & Reynolds (1998) and Lundell (2007), Lundell, Monokrouses & Brandt (2009) numerically demonstrated the benefit of system identification in improved controller implementation over the *ad hoc* methods previously implemented. Furthermore, Lundell *et al.* (2009) highlighted the difficulty associated with current actuators (e.g. suction) and suggested that available actuator technology is a significant limitation in boundary layer control efforts. A comprehensive review of actuators for flow control is provided by Cattafesta & Sheplak (2011). Toward resolving this limitation and the implementation of streak control, in a precursor to the present work, Hanson *et al.* (2010) and Osmokrovic, Hanson & Lavoie (2015), demonstrated that plasma actuator arrays could be used to effectively reduce the energy contained within targeted modes of spanwise-periodic streak disturbances generated using a static array of roughness elements at steady state. Furthermore, Hanson *et al.* (2014) provide an experimental demonstration of feedback control using a proportional integral (PI) controller which actively senses and controls steady and slowly varying streak disturbances introduced by a spanwise array of roughness elements. Targeting the fundamental mode disturbance for reduction (based on the roughness-element spacing), the mode's disturbance energy is shown to be reduced by 94 % at the feedback sensor location in Hanson *et al.* (2014). Osmokrovic *et al.* (2015) provided an investigation into the geometry and operating parameters used in dielectric barrier discharge plasma actuators, similar to those used here.

The present research demonstrates the control and mitigation of unsteady streaks that are generated in the boundary layer by a dynamically activated roughness element; both feedforward and feedback control are used. Furthermore, a comprehensive assessment of the limited control bandwidth is made. This work builds upon the steady/slowly varying feedback disturbance control of Hanson *et al.* (2014). To minimize the complexity of the experimental arrangement, a model problem is considered where a localized, rather than spanwise periodic, disturbance is produced using a single roughness element that is controlled by a pair of single-dielectric-barrier-discharge (SDBD) actuators. However, the caveat of this method is that it becomes difficult to match the spatial distribution of the roughness and actuator disturbances such that it is not possible to control the streak disturbance over the entire spatial domain of interest. Therefore, the inputs to the controller are from a single representative spanwise location within the streaks. This does not imply a limitation since the effectiveness of attenuation of streaks over the entire spatial domain using multiple spanwise-periodic SDBD actuators has already been successfully demonstrated by Hanson *et al.* (2014) for spanwise-periodic steady streaks; the present study aims to incorporate added complexity, focusing on the unsteadiness of streaks. In the case of a spanwise-periodic actuator array, it is possible to, for example, match the spanwise profile of the streak disturbance one Fourier mode at a time. Since the temporal dynamics of controlling a single or multiple streaks is expected to be similar, the present isolated disturbance experiment provides an efficient means to assess the dynamics of the control system for disturbances of a time scale comparable to the convective time scale over the spatial control domain. Nonetheless, the target overarching implementation is a distributed control system, where the control is achieved over the entire boundary layer with sufficient bandwidth.

Leading toward the active real time control of dynamic streak disturbances, this paper first demonstrates the undisturbed and disturbed boundary layer flow structure in § 3. In § 4, which should be viewed as part 1 of the major contribution of this work, the boundary layer response to dynamic forcing by a roughness element and a plasma actuator are examined to develop response models, leading to the development of a feedforward–feedback control model. In part 2 of this work's major contributions, the results of implementing the controller under various forcing programs and controller variations are investigated in § 5, and in § 6, simulated disturbance control is examined to explore the theoretical limitations of the controller and the associated frequency response.

2. Experimental details

2.1. *Facility overview*

The experiments were carried out in a suction-type wind tunnel. The flow conditioning of the wind tunnel (four layers of 16-mesh screen, one layer of 6.35 mm honeycomb and five layers of 30-mesh screen) is followed by a 10.8:1 contraction and a 3 m long and 0.35 m square test section. The test section is followed by a diffuser and the upstream components are vibration isolated from the blower. During experiments the free stream velocity was varied between 4 and 6 m s^{-1}, for which the turbulence intensity based on the streamwise velocity fluctuations was less than 0.05 %.

A flat plate positioned within the test section, with the leading edge 1.6 m downstream of the tunnel contraction exit, was used to generate a Blasius boundary layer, identified here as the basic state flow. The plate was made from 12.7 mm thick, 0.635 m long Plexiglas which was fitted with a 63 mm long aluminium sharp leading edge, machined flat with the top side of the Plexiglas and to a 15° downward angle. A 150 mm long aluminium trailing edge flap was used to set the stagnation point location on the measurement side (Saric 2007). The plate was located between one-third and one-quarter of the test section height in order to minimize effects from contraction induced secondary flows, as recommended by Saric (2007). The plate was mounted to the wind tunnel floor and given a slight positive angle to achieve a zero pressure gradient over $-25 \leqslant x-x_k \leqslant 350$ mm; where $x_k = 150$ mm is the streamwise distance from the leading edge to the roughness-element centre. Figure 1 provides a schematic of the flat plate orientation and coordinate system with important features, components and dimensions.

2.2. *Controller overview*

The controller is designed to be sufficiently robust while retaining real time control capabilities. The streamwise shear stress acts as an input to the controller both upstream and downstream of the actuator, providing feedforward and feedback inputs, respectively. Although only a single sensor at each location does not resolve the spanwise variation of the streaks, the objective of this study is the temporal dynamics of the control system. A representative diagram of the architecture of the controller is shown in figure 2. During the experiments a single activated roughness element induces an unsteady disturbance that is detected by the upstream feedforward sensor. This provides input to the controller prior to the disturbance reaching the location of the actuator. The output of the controller determines the excitation signal to the plasma actuator, which provides the control action. Feedback information, obtained downstream of the actuator, is input to the controller to correct for error. An in-depth description of the model identification and subsequent model-based design of the controller is discussed in § 4.
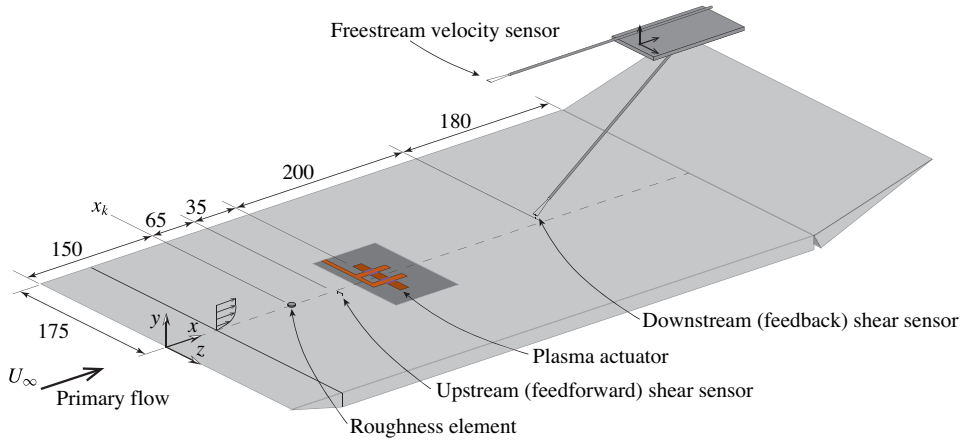
FIGURE 1. (Colour online) The arrangement of the control components relative to the flat plate, drawn to scale (all dimensions in mm).
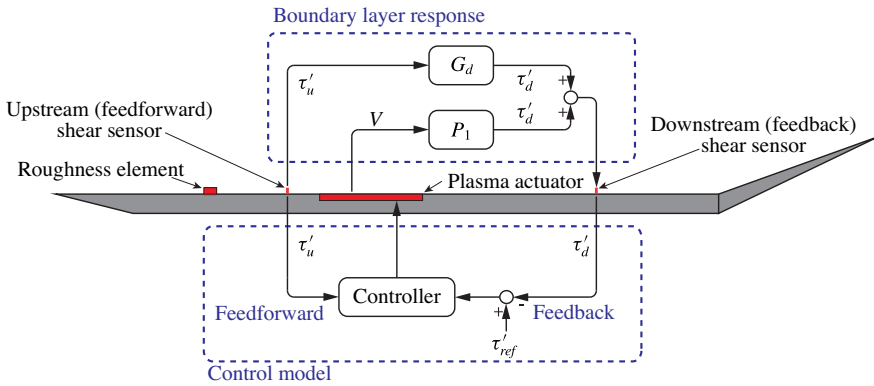

FIGURE 2. (Colour online) Block diagram of the primary control system components and a demonstration of the feedforward–feedback controller.

The system was implemented using a dSpace DS1103 PPC Controller Board operated by dSpace ControlDesk 4.2 software on a 64-bit PC. This system can accommodate up to 20 channels of differential A/D input, and up to 8 channels of differential D/A output. The 16-bit channel resolution adequately resolved the low-voltage signals provided by the shear stress signals. The control model was digitally constructed using MathWorks Simulink software, which was uploaded to the dSpace Controller Board using dSpace Real Time Interface.

2.3. *Roughness element*

A single cylindrical roughness element made from Teflon with a diameter, $D = 5.0$ mm, was used for this study. The roughness element had a fixed streamwise position relative to the leading edge of $x_k = 150$ mm. The roughness element was fixed to a servo piezoelectric Squiggle® motor located below the plate. The roughness-element deployment height above the plate surface, k, was controlled over a range of $0 \leqslant k \leqslant 1.5$ mm, to within ± 0.002 mm. The velocity and acceleration
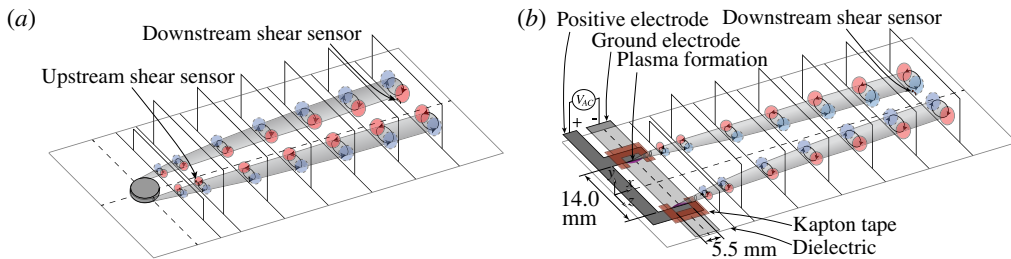
FIGURE 3. (Colour online) Schematic representation of the counter-rotating vortex pair and the associated streamwise velocity disturbance induced in the boundary layer by (*a*) an isolated roughness element and (*b*) a plasma actuator pair. Red/solid-outline: positive disturbance, blue/broken-outline: negative disturbance.

of the roughness-element motion (v_k and a_k respectively) was prescribed, and preliminary testing determined the maximum v_k and a_k to be: $v_k = 7.5$ mm s^{-1} and $a_k = 1000$ mm s^{-2}, such that additional instabilities were not excited. The roughness-element motion and height were verified with a laser position sensor.

For an undisturbed laminar boundary layer, a pair of counter-rotating vortices was generated downstream of the roughness element with $k < D$ and $k < \delta_{0.99}(x_k)$; as demonstrated experimentally by Pattenden, Turnock & Zhang (2005) and observed computationally by Visbal (1991) and Rizzetta & Visbal (2007). The two vortices are primarily aligned in the streamwise (*x*) direction such that they induce flow toward the wall on the inside (smaller $|z|$ region) and away from the wall on the outside (larger $|z|$ region). Figure 3(*a*) demonstrates this counter-rotating vortex pair arrangement schematically (and is supported by the hot-wire measurements in § 3). As high-speed fluid is drawn toward the wall, from larger y locations in the boundary layer, a positive disturbance is generated. Outboard of the positive regions, low-speed fluid is drawn away from the wall by the vortex pair resulting in negative disturbance regions; a process known as the lift-up mechanism, first identified by Landhal (1980). These streamwise-elongated regions of positive and negative disturbance velocity are the streak disturbances to be controlled in this study. In addition to these streaks, another prominent flow feature is the zone of low-speed fluid present in the wake of the element. This low-speed disturbance decays with downstream distance, leaving the streaks as the only significant disturbance persisting over the entire flow domain.

2.4. *Plasma actuator*

SDBD plasma actuators (hereafter simply referred to as plasma actuators), provide a uniquely deployable, robust and adjustable amplitude flow forcing that is appropriate for the target control experiments (Hanson *et al.* 2010, 2012, 2014; Osmokrovic *et al.* 2015). A comprehensive description of this type of a plasma actuator arrangement may be found in Corke, Post & Orlov (2009) or Benard & Moreau (2014). Plasma actuators were used to provide a counter-disturbance to the roughness-element-induced disturbance. The locations of the actuators are shown in figure 1. In order to introduce the desired flow disturbance to counteract the disturbance induced by the upstream roughness element, a single pair of spanwise forcing plasma actuators was used, as shown in figure 3(*b*), with the forcing from each actuator oriented toward the

other. This arrangement results in a pair of counter-rotating streamwise vortices, as demonstrated schematically in figure 3(*b*) and shown in detail by Jukes & Choi (2012, 2013). The result is low-speed streaks between the actuators with high-speed streaks on the outside, which are similar in shape but opposite in sign to the streaks generated by the isolated roughness element.

The spatial distribution of the plasma and the induced flow forcing is highly dependent on the geometry and arrangement of the electrodes, the dielectric material and its thickness and the driving supply voltage and frequency (Osmokrovic *et al.* 2015). The geometry of the high-voltage electrodes is shown in figure 3(*b*), and the outer side of each electrode was covered with Kapton tape to prevent plasma formation. The plasma actuator was operated with a high-frequency/high-voltage signal supplied from a Trek model 609C-6 high-voltage DC amplifier. The input to the amplifier was provided by an Agilent 33120A function generator producing a 4 kHz carrier sine wave with unity amplitude that was modulated by the output of the dSpace controller.

2.5. *Shear-stress sensors*

Wall-shear-stress sensors are employed for control implementation in order to avoid any flow interference that would result from measurement of velocity within the boundary layer. The spanwise wall-shear stress (τ'_z) is the ideal quantity to measure since the wall-normal velocity disturbance leading to the formation of the streaks is associated with an immediate spanwise wall-shear-stress signature (Naguib, Marrison and Zaki 2010), enabling sensing of the streaks without delay. However, the only practical way for measuring τ'_z relies on the use of two hot wires in a V-configuration, which has two limitations: first, the sensor detects both the streamwise (denoted here as τ') and the spanwise shear stress with measurement of the latter relying on the small difference between two large quantities that are dominated by τ'; and, second, the sensing 'volume' of the sensor is substantially larger than a single wire, resulting in appreciable attenuation of the measurement signal. These limitations are especially significant in the present application where focus is on the control of minute disturbances that are undergoing linear growth. Therefore, the present control implementation incorporates streamwise wall-shear-stress sensors. A drawback of this approach is that the τ' signature of a streak-produced disturbance lags behind the passage of this disturbance past a given x location (Naguib *et al.* 2010). This lag is undesirable but not detrimental. For the feedforward sensor, this means a minimum distance must be kept between the sensor and the actuator in order for the feedforward measurement to produce a control signal prior to the arrival of the streak at the actuator. For the feedback sensor, this lag adds phase delay in the control loop, and hence lower controller gains (i.e. slower control response), must be used if the phase margin of stability is to be maintained.

Two shear-stress sensors were used to provide feedforward and feedback information to the controller, and are noted in figures 1, 2 and 3(*a*,*b*). Each sensor was a single hot-wire sensor with 5 µm diameter tungsten wire and a 1 mm active length oriented to measure the streamwise shear-stress magnitude. The sensors were operated with Dantec MiniCTA 54T30 constant temperature anemometers, at an overheat ratio of 0.5. The output of each anemometer was passed through a 20 Hz low-pass fourth-order Butterworth analog filter. The shear-stress sensors were calibrated at 10 discrete shear-stress values spanning the range encountered during the experiments. A second-order polynomial was fit to the calibration data for each sensor.

Each sensor was placed within the linear region of the undisturbed Blasius boundary layer velocity profile and within the expected location of a high-speed streak disturbance generated by the roughness element. The upstream (feedforward) sensor was constructed with the probe prongs passing through a plug that fit flush with the flat plate surface at $(x_{ff}-x_k, y, z) = (65, 1.0, -1.5)$ mm. The downstream (feedback) sensor utilized one of the four roving hot-wire sensors (§ 2.6) at $y_{fb} = 1.5$ mm, and $z_{fb} = 2.5$ mm; and $x_{fb}-x_k = 125, 200, 250$ or 300 mm. For the experiments leading to the data presented in figure 18(c,e,g,i,k), where the roving wires were required to capture the flow state, a feedback hot-wire sensor was constructed similar to that of the feedforward sensor, and placed at $(x_{fb}-x_k, y, z) = (300, 1.5, 2.5)$ mm.

2.6. *Hot wires*

The primary method of flow-state measurement was an array of four single-wire hot-wire probes that were used to measure the streamwise velocity. The streamwise velocity was sampled over seven x–y planes at x–$x_k = 25, 50, 100, 150, 200, 250$ and 300 mm, across a spanwise extent of $-19 \leqslant z \leqslant 20$ mm and over $0.1 \lesssim y \lesssim 12$ mm; where $(x-x_k, y, z) = (0, 0, 0)$ is defined as the centre of the roughness element on the flat plate surface. Boundary layer profiles were acquired at 1 mm steps along the span, and the wall-normal spacing of the points varied in order to sufficiently resolve the boundary layer velocity gradients. Each probe had a 5 μm diameter, 1 mm long tungsten sensor, and the four sensor centres were set at 5 mm spanwise increments, all at the same x and y location. An overhead 3-axis traverse was used to position the four-hot-wire-probe array within the wind tunnel. The hot-wire signals were acquired using a National Instruments BNC-2012 board and DAQ-6061 analog-to-digital card. TSI 1054 A/B constant temperature anemometers were used to operate the four hot wires with an overheat ratio of 0.5. Ambient temperature compensation (Lemonis & Dracos 1995) was implemented to account for the 21 ± 3 °C variations. The hot-wire calibrations were performed above the plate in the free stream of the wind tunnel, where a pitot tube provided the reference velocity. King's Law was fit to the calibration data of twelve free stream velocities ranging from $1.0 \leqslant U_\infty \leqslant 6.0$ m s^{-1}. Pre- and post-calibrations were within 1 %.

At each measurement location, a 50 s time series was acquired at 10 kHz, which allowed for 25 cycles of a 2 s roughness-element actuation period (at 50 % duty cycle). The use of an actuating roughness element allowed for steady state, undisturbed (roughness element withdrawn) and disturbed (roughness-element deployed) flows, to be measured in a single time series, along with the unsteady disturbance growth during the roughness-element motion. In post-processing, the 25 cycles were phase averaged relative to the roughness-element position sensor signal. At each spanwise location, the wall location was inferred from a least-squares linear fit of each y profile over the linear portion of the undisturbed velocity profile. An additional single hot wire was permanently positioned in the free stream (see figure 1) in order to adapt the Blasius boundary layer shear-stress control target (i.e. set point) to variation in free stream velocity. This hot wire was operated by a TSI 1750 anemometer with the same overheat and calibration methodology as previously described.

3. Flow state without control

A Blasius boundary layer was established as the basic state at three free stream velocities of $U_\infty \approx 4.0, 5.0$ and 6.0 m s^{-1}. The free stream turbulence intensity based on the streamwise velocity was ≈ 0.02 %. Figure 4(a) demonstrates the self-similar
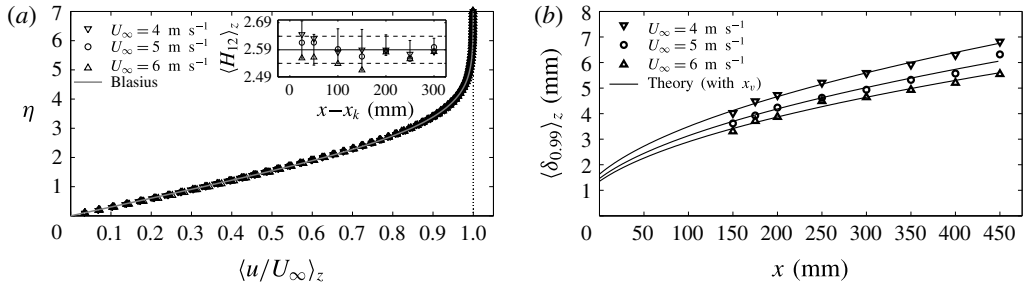
FIGURE 4. (a) Blasius basic state, measured boundary layer profiles at x–$x_k = 25$, 50, 100, 150, 200, 250 and 300 mm for the three free stream velocities; the inset figure demonstrates the corresponding shape factors. (b) The measured boundary layer thickness.

profiles of the measured boundary layer where the wall-normal coordinate, η, is given by

$$\eta = \frac{y}{\delta}, \quad \text{where } \delta = \sqrt{\frac{\nu(x - x_v)}{U_\infty}} \text{ and } x_v = \left(\frac{\delta^*}{1.721}\right)^2 \frac{U_\infty}{\nu}, \quad (3.1)$$

and δ is the Blasius similarity length scale, x_v is the virtual boundary layer origin location and δ^* is the displacement thickness. The values of each are spanwise averaged over the measurement domain, denoted with $\langle \rangle_z$. To quantitatively compare the undisturbed boundary layer profile to the Blasius solution, the shape factor, $H_{12} = \delta^*/\theta$, is typically employed; where θ is the momentum thickness. According to Saric (2007), the recommended Blasius shape factor is 2.59 ± 0.005, while in practice ± 0.05 is typical (White 2002; Lundell 2007). The inset of figure 4(a) provides the spanwise-averaged shape factor, $\langle H_{12} \rangle_z$, at each velocity (symbols) with error bars representing the range measured for all cases, which are in good agreement with a Blasius boundary layer. Furthermore, the measured boundary layer thickness shown in figure 4(b) follows the corresponding Blasius solution and was found to be $3.3 \leqslant \delta_{0.99}(x) \leqslant 7.0$ mm over the streamwise domain of the measurements. At the roughness-element location, x_k, the boundary layer thickness varied from $3.3 \leqslant \delta_{0.99}(x_k) \leqslant 4.0$ mm. Notably, the roughness-element height range investigated here, $0 \leqslant k \leqslant 1.5$ mm, was typically within the nominally linear range ($u/U_\infty \leqslant 0.35$) of the undisturbed profile.

Hot-wire measurements of the disturbance velocity at different y–z planes over the streamwise region of interest provide details of the disturbance size, strength and spatial profile; both while the roughness element is in motion and at steady state. Results are acquired at seven streamwise planes, with $x_k = 150$ mm. A representative set of measurements with $k = 1.29$ mm and $U_\infty = 5.0$ m s^{-1} is provided in figure 5 to demonstrate the spatio-temporal roughness-element-induced disturbance growth. The peak positive disturbance amplitude is found to be $u'/U_\infty = 11.6\%$ at steady state for $k = 1.29$ mm, and $u'/U_\infty = 13.6\%$ at steady state for the highest roughness-element at $k = 1.4$ mm. In panel (a), the roughness-element height versus time is provided with markers indicating the five time instants where the disturbance measurements are provided (t_1–t_5). The disturbance is observed to grow in strength in each subsequent plane as time progresses.
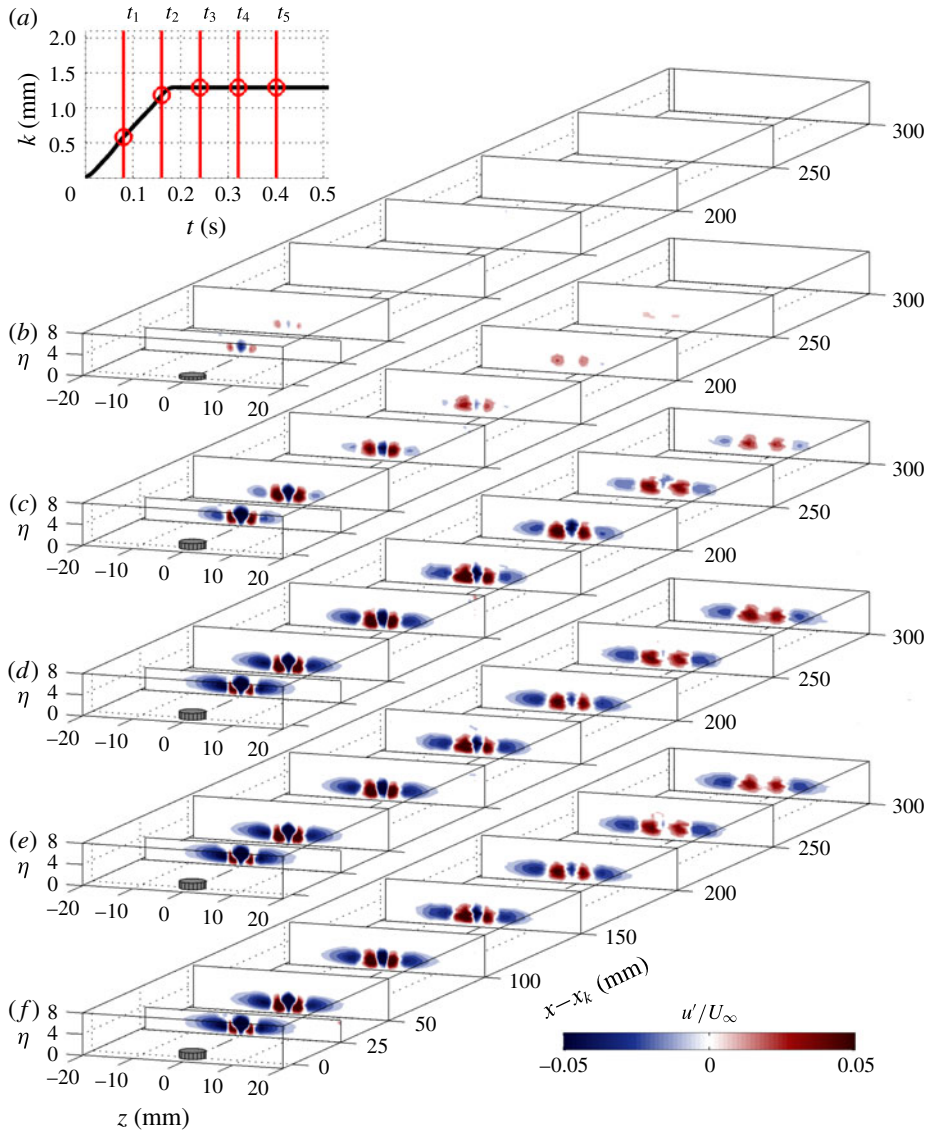
FIGURE 5. (Colour online) Unsteady streamwise velocity disturbance contours with a roughness element deployed from $k = 0$ to 1.29 mm at five instants in time. The roughness-element height versus time is provided in (a) where the five time instants ((b) t_1, (c) t_2, (d) t_3, (e) t_4, (f) t_5), corresponding to the disturbance contour results are labelled. The maximum positive disturbance at steady state is 11.6%.

The disturbance shape is qualitatively similar for all k and U_∞ combinations, with an increasing disturbance strength with k and U_∞ (for further details see Bade 2014); furthermore, all presented parameter combinations produce non-transitional streaks within the measurement domain. The existence of a low-speed region, centred downstream of the roughness element, and elevated from the wall, is apparent in all cases. This wake region appears between two high/low speed disturbances that are presumed to be generated by the counter-rotating vortex mechanism depicted in
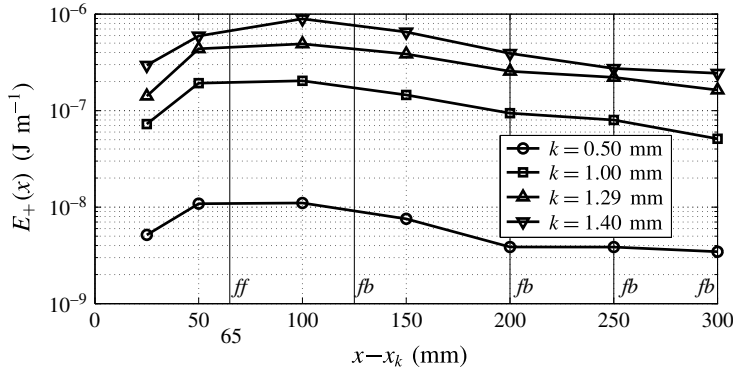
FIGURE 6. Streamwise evolution of the positive streak disturbance energy, E_+, for $D = 5.0$ mm and $U_\infty = 5.0$ m s^{-1} with $k = 0.5$, 1.0, 1.29 and 1.4 mm. Noted is the streamwise location of the feedforward (*ff*) sensor, as well as the different feedback (*fb*) sensor locations.

figure 3(*a*). For all cases, the low-speed wake region experiences a slow decay with x, nearly disappearing by $x–x_k \approx 300$ mm. For all k, the disturbance spreads in the span as well as the wall-normal direction (in dimensional terms) with increasing x. The wall-normal growth is more substantial within $25 \leqslant x–x_k \leqslant 100$ mm, and slows for $x–x_k > 100$ mm. Figure 6 depicts the streamwise evolution of the energy of the high-speed streak at steady state calculated using

$$E_+(x) = \frac{\rho}{2} \int_z \int_y u'_+(x, y, z)^2 \, \mathrm{d}y \, \mathrm{d}z \quad \text{and} \quad u'_+ = \begin{cases} u' & \text{if } u' > 0, \\ 0 & \text{if } u' < 0, \end{cases} \quad (3.2a,b)$$

where E_+ is the energy of the positive disturbance per unit streamwise length. The integral (3.2*a,b*) is carried out only over the region where the disturbance is positive. As seen from figure 6, the energy of the high-speed streak initially grows with downstream distance to reach a peak in the region $x–x_k = 50$–100 mm, depending on the roughness height, before decaying with further increase in x. As would be expected, the streak energy increases with increasing roughness height. Also, marked on the plot in figure 6 is the location of the feedforward sensor and the different locations of the feedback sensor. As seen from the figure, the feedforward sensor is always located within the domain where the streak energy grows or peaks. On the other hand, the feedback sensor is located within the energy decay zone, with the most upstream location, $x_{fb}–x_k = 125$ mm, being near the position of peak energy, at the start of energy decay. It was not possible to move the feedback sensor further upstream without risking potential interference with the measurement signal from the plasma actuator.

The temporal development of the disturbance at $x–x_k = 305$ mm, is highlighted in figure 7 which shows the planar development of the disturbances in time. These results verify the characteristics of the target disturbance for control: dynamic streaks with prescribable location, strength and spatial distribution. It is noteworthy that these streaks do not replicate the detailed complexity of streaks in bypass boundary layer transition; e.g. a high-speed streak following a low-speed streak (the exemplified scenario is significant to the development of the so-called inner instability, where
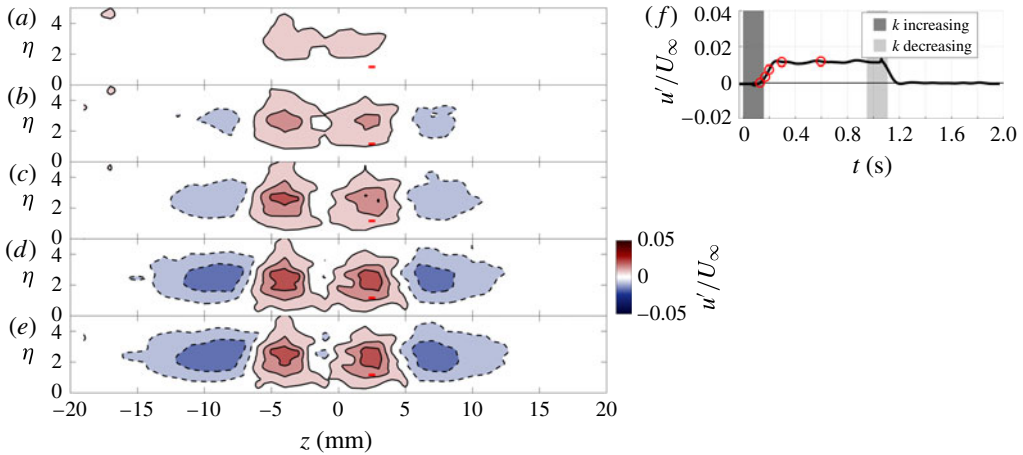
FIGURE 7. (Colour online) Unsteady disturbance development in time at $x-x_k = 305$ mm in the y–z plane, induced by the roughness element deployed from $k = 0$ to 1.2 mm. The feedback sensor, located at $(x_{fb}-x_k, y, z) = (300, 1.5, 2.5)$ mm is indicated by a rectangle. Panel (f) provides the normalized velocity disturbance at the y–z location of the feedback sensor with time; five time instants are marked corresponding to the five disturbance contours ($t = 0.13$ s (a), 0.17 s (b), 0.20 s (c), 0.30 s (d), 0.60 s (e)).

the low- and high-speed streaks overlap (Vaughan & Zaki 2011)). The 'synthetic' streaks utilized here are either low or high speed, and hence do not reproduce such scenarios. Nevertheless, this does not impose a limitation in evaluating the viability of the control strategy. In particular, this situation is akin to using information learned from a step-response test to judge if a control system is sufficiently fast to control a sine wave disturbance of particular frequency. Similarly, if successful control is demonstrated for a low- or a high-speed streak in isolation, one would expect the control to work satisfactorily if a high-speed streak follows a low-speed streak, or *vice versa*, provided that both streaks have comparable time scale to the isolated streak. Although, in this case, the control of both low- and high-speed disturbances at the same spanwise location would require modification of the present actuator to allow for introducing bi-polar control disturbances. This can be achieved, for example, by using a second actuator immediately downstream of the present actuator with similar geometry but shifted along the span such that the high-voltage electrodes of the two actuators form a staggered arrangement.

The disturbance induced by the plasma actuator was investigated in the y–z plane at $x-x_k = 305$ mm. The resulting temporal development of the disturbances is shown in figure 8 for $V = 2.4$ kV and $U_\infty = 5.0$ m s^{-1}. The disturbance shape is qualitatively similar for all (non-transitional) voltages, V, and the disturbance intensity increases with V. The spatial variation of these disturbances are similar to that induced by the roughness element, but opposite in sign. Disturbances of slightly different strength in the positive and negative z half-planes are observed, an unintended consequence of using Kapton tape to establish the actuator length, apparently resulting in slightly different actuator lengths. Because the feedback sensor was positioned in the $+z$ half-plane, the control assessment will focus on this region. As prescribed, the feedback sensor is located within the negative streak region of the plasma actuator-induced disturbance, as noted in figure 8.
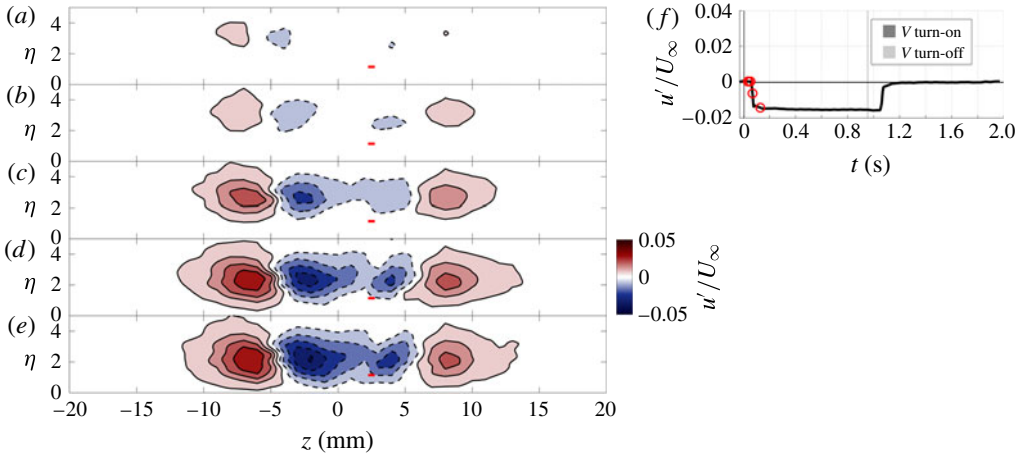
FIGURE 8. (Colour online) Unsteady disturbance development in time at $x-x_k = 305$ mm in the y–z plane, induced by the plasma actuator with an input signal modulated from $V = 0$ to 2.4 kV. The feedback sensor, located at $(x_{fb}-x_k, y, z) = (300, 1.5, 2.5)$ mm, is indicated by a red rectangle. The panel (f) provides the normalized velocity disturbance at the y–z location of the feeedback sensor with time; five time instants are marked corresponding to the five disturbance contours ($t = 0.03$ s (a), 0.04 s (b), 0.05 s (c), 0.07 s (d), 0.13 s (e)).

4. Controller development

A feedforward–feedback controller was implemented, in which the measured upstream shear stress (τ'_u) was used for feedforward control, and the measured downstream shear stress (τ'_d) was used for feedback control; the voltage amplitude for the plasma actuator was used as the control variable (i.e. the 'plant input'). Simple linear models were identified from experimental measurements, as described below, and these models were then used to design suitable parameters for the controllers. A schematic of the overall control architecture is shown in figure 9.

4.1. *Linear models for boundary layer response*

In figure 9, the dashed block labelled P represents the model of the 'plant' (the system to be controlled): the input to this block is a control signal f (related to the voltage applied to the plasma actuator, as described below), and the output is the effect the plasma actuator has on the downstream shear stress τ'_d. The goal of actuation is to counteract the effect the upstream disturbance τ'_u has on the downstream shear stress; this effect is represented by the transfer function G_d in the block diagram.

In our study, we assume G_d is simply a constant gain K_τ with a convective time delay t_τ:

$$\frac{\tau'_d(s)}{\tau'_u(s)} = G_d(s) = K_\tau e^{-t_\tau s}, \qquad (4.1)$$

where $\tau'_u(s)$ and $\tau'_d(s)$ denote the Laplace transform of the upstream and downstream shear stress, respectively. The model parameters K_τ and t_τ were determined from experimental data, by deploying the roughness element from wall flush to multiple prescribed roughness-element heights, which provided an approximate step response
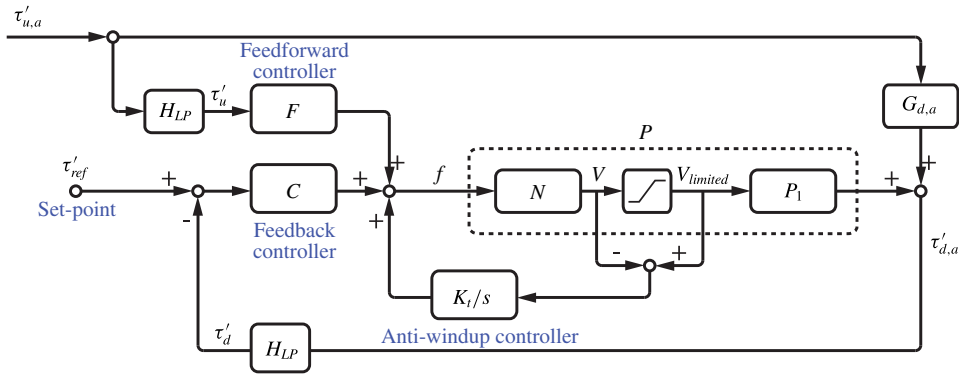
FIGURE 9. (Colour online) Block diagram of the boundary layer response models and the feedforward–feedback controller.

$x_{fb}-x_k$ (mm)	K_τ	t_τ (s)
125	0.9940	0.0325
200	0.4433	0.0485
250	0.3122	0.0722
300	0.2249	0.0909

TABLE 1. Summary of the gain, K_τ, and time delay, t_τ, parameters determined for the model G_d from (4.1), with various feedback sensor positions, $x_{fb}-x_k$.

over a range of amplitudes. The roughness element was held at the fully up/down locations for approximately 1 s, resulting in one up/down cycle period of 2 s. Approximately 25 cycles were phase averaged for each roughness-element height to remove small cycle-to-cycle differences. The 25-cycle average produced steady state disturbances with 1 % and 2 % uncertainty, based on the r.m.s. of the deviation of the individual I/O signals of the upstream and downstream shear stress, respectively. Figure 10 shows the phase-averaged results for the $k = 0$ to 1.2 mm case, as well as the simple linear model. The gain K_τ, is calculated as the ratio of the downstream to upstream disturbance shear-stress values at steady state. The time delay, t_τ, which is primarily representative of the convection time for the disturbance to travel from the upstream to the downstream shear-stress sensor, is determined as the time difference when the disturbance reaches 10 % of its steady-state value at each sensor. Figure 11 shows the values of K_τ and t_τ determined at each discrete roughness height k. The parameter values are relatively independent of the amplitude k, justifying the use of the linear model (4.1). Table 1 gives the values of K_τ and t_τ at four different streamwise locations for the feedback sensor.

Next, the model for the effect of the plasma actuators on the downstream shear stress is developed, which is represented by the dashed box labelled P in figure 9. To determine such a model, experimental measurements of step responses were again acquired, an example of which is shown in figure 12.

The step-response data were acquired with the actuator driven by a square wave with a 2-second period, which modulated a 4 kHz sine wave at several amplitudes between 1.6 and 2.6 kV. Approximately 25 cycles were phase averaged, and a sample response is shown in figure 12, for a voltage of $V = 2.4$ kV; as stated previously, the
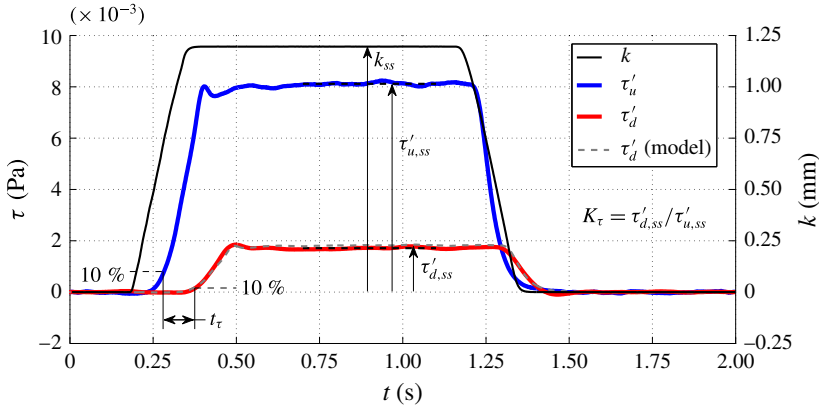
FIGURE 10. (Colour online) Example phase-averaged step-response data for determination of the parameters in the boundary layer response model G_d, with $k = 0$ to 1.2 mm, and the feedback sensor at $x_{fb}-x_k = 300$ mm.
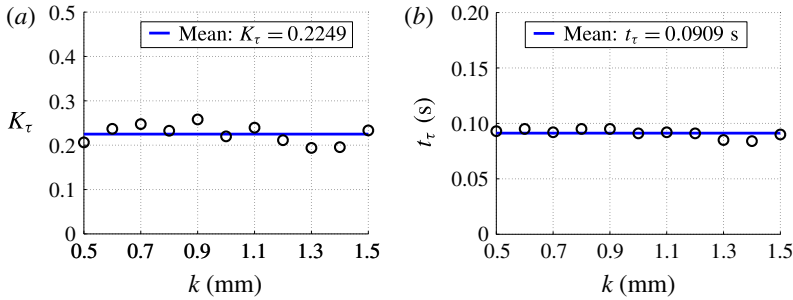

FIGURE 11. (Colour online) Parameters for the model G_d from (4.1): (*a*) gain, K_τ and (*b*) time delay, t_τ, with the feedback sensor at $x_{fb}-x_k = 300$ mm.

uncertainty of the downstream shear stress was 2 % of the steady-state disturbance. Figure 13(*a*) demonstrates the relationship between the plasma actuator voltage amplitude and the steady-state downstream shear-stress disturbance. As seen in the figure, there is a range of plasma actuator voltage, larger than the plasma minimum turn-on voltage ($V = 1.6$ kV), where the induced downstream shear-stress disturbance is independent of the voltage ($1.6 \leqslant V \leqslant 2.35$ kV). For higher voltages, the disturbance monotonically increases, until turbulent spots are induced for voltages above 2.6 kV. Therefore, the useful range of actuation voltage was $2.35 \leqslant V \leqslant 2.6$ kV, for this particular actuator and the flow conditions of these experiments; these voltages are denoted by the data points represented by circles in figure 13(*a*).

For control design, a simple model for the effect of the plasma actuators on the downstream shear is to be determined. In the block diagram in figure 9, the block P_1 represents the mapping from voltage V supplied to the plasma actuator, to the resulting perturbation τ'_d in the downstream shear stress (as shown in figure 12). Note that, for actuation voltages from 2.35 to 2.6 kV, the response does appear linear (figure 13*a*), but there is a deadband (since there is no measurable effect for voltages below 2.35 kV), so the response is actually nonlinear. We remedy this by defining a new control variable f, which is simply the voltage scaled and shifted to eliminate
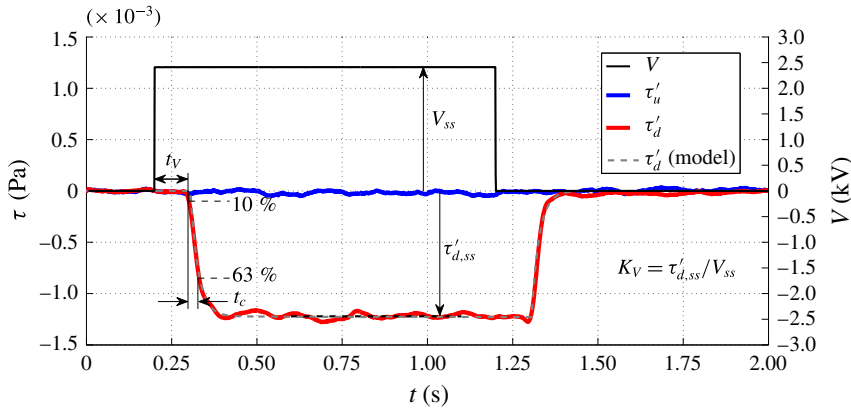
FIGURE 12. (Colour online) Sample phase-averaged step-response data for determination of the boundary layer response model (P) parameters with $V = 0$ to 2.4 kV with the feedback sensor at $x_{fb} - x_k = 300$ mm.
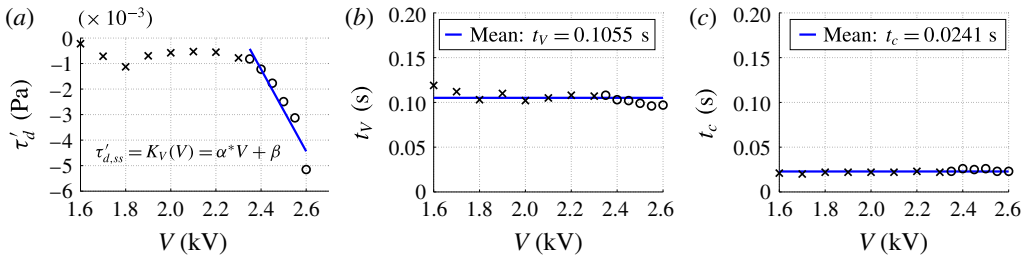

FIGURE 13. (Colour online) Plant model, P_1, parameters for the (a) gain, $K_V(V)$; (b) time delay, t_V; and (c) time constant, t_c, with the feedback sensor at $x_{fb} - x_k = 300$ mm. Symbols ∘ and × denote used and unused voltages, respectively.

the deadband. In particular, from figure 13, we see that within the useful range of actuation, the steady-state shear-stress perturbation is well approximated by

$$\tau'_d = \alpha V + \beta. \tag{4.2}$$

The control variable is then defined to be $f(t) = \alpha V(t) + \beta$, so that the relationship between f and τ'_d is approximately linear. The voltage is then easily determined from f according to

$$V = N(f) := (f - \beta)/\alpha, \tag{4.3}$$

and this static nonlinear map is denoted by the block N in figure 9.

The transfer function from the shifted/scaled voltage f to the downstream shear stress is represented as a first-order lag with delay:

$$\frac{\tau'_d(s)}{f(s)} = P(s) := \frac{e^{-t_V s}}{t_c s + 1}, \tag{4.4}$$

represented by the dashed block P in figure 9. One final complication is that, in practice, the voltage to the plasma actuator is limited by some maximum voltage. The resulting saturation nonlinearity is also indicated in the block diagram.

$x_{fb}-x_k$ (mm)	t_V (s)	t_c (s)	α	β
125	0.0292	0.0242	-0.00575	0.0132
200	0.0595	0.0198	-0.0278	0.0664
250	0.0814	0.0196	-0.0152	0.0356
300	0.1055	0.0241	-0.0170	0.0389

TABLE 2. Summary of the time delay, t_V, time constant, t_c and gain fit coefficient, α and β, parameters determined for the plant model P in (4.4), for various feedback sensor positions, $x_{fb}-x_k$.

In the model (4.4), the time delay t_V is defined as the time between the plasma actuator voltage reaching 2 % of the max value, and the time at which the downstream shear stress reaches 10 % of its steady-state value (as shown in figure 12). These threshold values were selected to conservatively ensure each is well above the noise level present on the measurement signals when the boundary layer is undisturbed. The time constant t_c was calculated as the time for the downstream shear-stress disturbance response to rise from 10 % to 63 % of the steady-state level. Figure 13(b,c) displays the values of t_V and t_c respectively for different forcing amplitude levels, which are approximately insensitive to the amplitude level. A summary of the parameters of (4.2)–(4.4) is found in table 2 for each of the four feedback sensor locations considered.

4.2. *Control design*

The controller consists of a feedforward component F and a feedback component C, as shown in figure 9. The feedforward component of the controller, F, takes the measured upstream disturbance shear-stress input and outputs a control contribution, f_{ff}. Similarly, the feedback component of the controller, C, takes the measured downstream disturbance shear-stress input and outputs a control contribution, f_{fb}. The control set point is noted as τ'_{ref} in figure 9, which corresponds to the target shear stress relative to Blasius value at the downstream shear-stress sensor. Theoretically, one wants the downstream shear to match the Blasius value, so one should take $\tau'_{ref} = 0$; in practice, τ'_{ref} was actively adjusted in real time to account for small free stream variations using a hot wire positioned in the free stream; this correction was found to be negligible, but would provide a more appropriate Blasius target in a less ideal setting.

The ideal feedforward control output is a disturbance of equal magnitude but opposite sign to that of the roughness-element-induced disturbance. Referring to figure 9, disturbance cancellation by feedforward control is achieved when

$$F(s)P(s) = -G_d(s). \tag{4.5}$$

From the models (4.1) and (4.4), it is clear that

$$F(s)\frac{e^{-t_V s}}{t_c s + 1} = -K_\tau e^{-t_\tau s} \tag{4.6}$$

and the resulting feedforward transfer function is

$$F(s) = -K_\tau(t_c s + 1)e^{-(t_\tau - t_V)s}. \tag{4.7}$$

Because the time delays t_τ and t_V are similar, the exponential term in (4.7) was omitted. In addition, the time constant, t_c, was ignored in designing the controller in the interest of simplicity (the implications of these approximations are discussed in detail in § 6). Thus, the feedforward controller has the particularly simple form of a constant gain

$$\frac{f_{ff}(s)}{\tau'_u(s)} = F = -K_\tau. \tag{4.8}$$

Table 3 provides the resulting values of the feedforward gain ($K_{ff} = K_\tau$) for the model developed at each streamwise feedback sensor location.

For the feedback controller, a proportional integral (PI) feedback controller was employed:

$$\frac{f_{fb}(s)}{\tau'_d(s)} = C(s) := K_{fb}\frac{t_I s + 1}{t_I s}. \tag{4.9}$$

The gains K_{fb} and t_I were determined from the plant model P, using the tuning rules and recommendations of Skogestad (2004), where the feedback integral time is determined by:

$$t_I = \min\{t_c, 8t_V\}. \tag{4.10}$$

In the plant model, the time constant is always smaller than the time delay (see table 2), and hence it was selected as the integrator time, for all streamwise locations of the feedback sensor. The feedback controller gain is calculated as

$$K_{fb} = \frac{0.5}{k_{fb}}\frac{t_c}{t_V}, \tag{4.11}$$

where $k_{fb} = 1$, for all streamwise locations of the feedback sensor. The resulting feedback gain and integral time values at each streamwise feedback sensor location are given in table 3. As expected, K_{fb} increases as x_{fb} decreases, due to the reduced convection time over the shorter streamwise distance. Finally, to prevent error accumulation in the integral portion of the feedback controller when the required control voltage was outside the available voltage range ($2.35 \leqslant V \leqslant 2.6$ kV), an anti-windup (Astrom & Murray 2010) controller, K_t/s, was included (see figure 9). The anti-windup term takes the form of an integrator with a gain that is tuned with the feedback controller's integral time, t_I, *viz*,

$$K_t = \frac{1}{k_t t_I}, \tag{4.12}$$

where $k_t = 4$ is used, a value determined by trial and error in order to achieve sufficient windup correction speed, while avoiding instability. Table 3 provides the feedforward and feedback controller parameters used in the control model at four discrete downstream shear-stress sensor locations.

5. Control results

Control experiments were carried out as outlined in table 4. The roughness-element height, free stream velocity, control strategy, streamwise location of the feedback sensor and roughness-element actuation frequency were independently varied to evaluate the effectiveness of the control model at these different conditions. All results are phase averaged relative to the roughness element motion, using a minimum of

$x_{fb}-x_k$ (mm)	K_{ff}	K_{fb}	t_I (s)	K_t
125	0.9900	0.4145	0.0242	10.33
200	0.4433	0.1664	0.0198	12.63
250	0.3122	0.1204	0.0196	12.75
300	0.2249	0.1141	0.0241	10.37

TABLE 3. Summary of the feedforward gain, K_{ff}, feedback gain, K_{fb}, feedback integral time, t_I and windup gain, K_t, parameters determined for the controllers, for various feedback sensor positions, $x_{fb}-x_k$.

Test cases (TC)	k (mm)	U_∞ (m s^{-1})	Control strategy	$x_{fb}-x_k$ (mm)	t_h/f_k (s)/(Hz)
1–6	$0 \rightarrow 0.5,\ 1.0,\ 1.1,\ 1.2,\ 1.3,\ 1.4$	5	$ff + fb$	300	2.0/0.25
7, 10	$0 \rightarrow 1.0,\ 1.4$	4	$ff + fb$	300	2.0/0.25
8, 11	$0 \rightarrow 1.0,\ 1.4$	5	$ff + fb$	300	2.0/0.25
9, 12	$0 \rightarrow 1.0,\ 1.4$	6	$ff + fb$	300	2.0/0.25
13 (repeat)	$0 \rightarrow 1.0$	6	$ff + fb$	300	2.0/0.25
14, 17, 20	$0 \rightarrow 1.0,\ 1.2,\ 1.4$	5	ff	300	2.0/0.25
15, 18, 21	$0 \rightarrow 1.0,\ 1.2,\ 1.4$	5	fb	300	2.0/0.25
16, 19, 22	$0 \rightarrow 1.0,\ 1.2,\ 1.4$	5	$ff + fb$	300	2.0/0.25
23, 24, 25, 26	$0 \rightarrow 1.2$	5	$ff + fb$	125, 200, 250, 300	2.0/0.25
27	$1.0 \rightarrow 1.2$	5	$ff + fb$	300	0.05/6.06
28	$1.0 \rightarrow 1.2$	5	$ff + fb$	300	0.1/3.85
29	$1.0 \rightarrow 1.2$	5	$ff + fb$	300	0.2/2.00
30	$1.0 \rightarrow 1.2$	5	$ff + fb$	300	0.5/0.93
31	$1.0 \rightarrow 1.2$	5	$ff + fb$	300	2.0/0.25

TABLE 4. Summary of test parameters for the control experiments. Subsets of experiments investigate the effect of the particular parameter highlighted in grey.

20 cycles. The investigation focuses on the ability of the control model to properly cancel/reduce the strength of the streak disturbance at the downstream location of the feedback sensor. Results were collected with and without control, and all results (except those featured in § 5.5) correspond to a prolonged hold time, $t_h \approx 2.0$ s, at the fully retracted and fully deployed roughness-element heights, allowing for steady and unsteady control evaluations.

5.1. *Effect of roughness-element height*

Figure 14 demonstrates the roughness-element motion from $k = 0$ to the various fully deployed roughness-element heights noted in table 4. The roughness-element motion time bands are provided for $k = 0$ to 1.4 mm in figure 14 and are provided for the appropriate k motion on all subsequent control results plots for reference.

For cases 1–6, the variation of the shear stress measured by the feedback sensor, τ_d', is shown in figure 15. Note that the total shear stress, base flow plus disturbance, remains positive for all measurements. Thick lines represent cases with control, $\tau_{d,\mathscr{C}}'$, whereas the corresponding style thin lines are without control. At the lowest
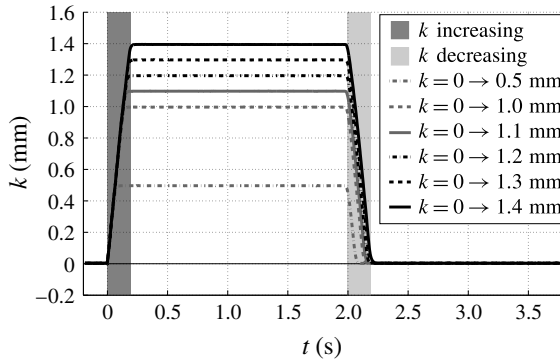
FIGURE 14. Dynamic (unsteady) roughness-element motion from $k = 0$ to various deployment heights, k. The grey bands demonstrate time periods when the roughness element is in motion, either upward or downward (shown for $k = 0$ to 1.4 mm here).
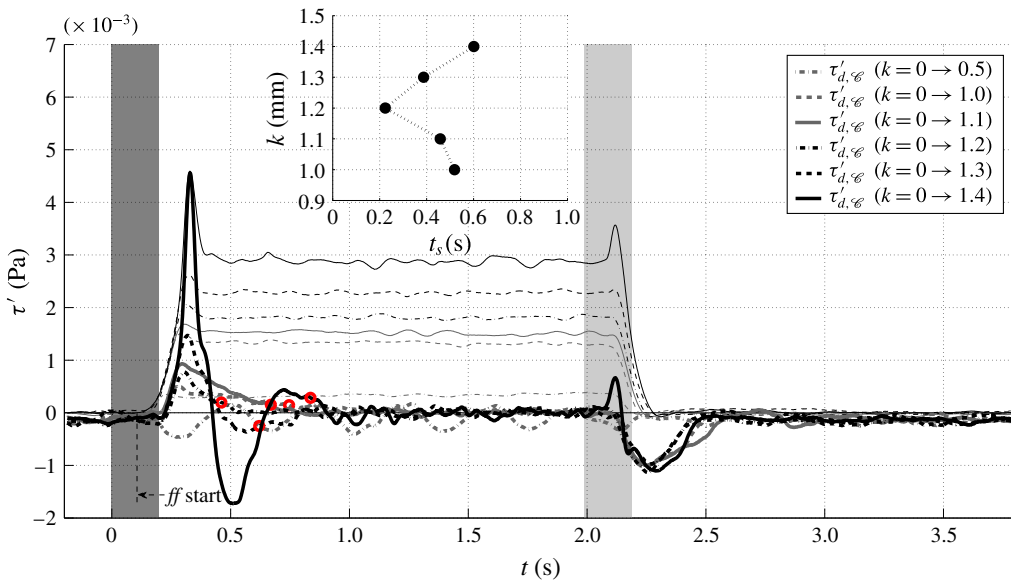

FIGURE 15. (Colour online) Unsteady control results for the downstream shear stress at various roughness-element heights with the feedback sensor at $x_{fb} - x_k = 300$ mm and $U_\infty = 5.0$ m s^{-1}. Uncontrolled- and controlled-flow cases are depicted using thin and thick lines respectively. The settling time for each signal is marked, and the inset provides the values for each controlled disturbance.

roughness deployment height, $k = 0.5$ mm, the uncontrolled disturbance level is near the minimum controllable shear stress. As a result, small disturbance fluctuations cause the controller to turn the actuator on and off intermittently resulting in under and over forcing of the boundary layer, and oscillations around the zero disturbance level ($\tau'_d = 0$).

At the larger roughness-element deployment heights, the controller effectively drives the disturbance shear stress to zero after sufficient time. For $k = 0$ to 1.0 and 1.1 mm the response of the controlled disturbance slowly reaches the zero level without

oscillations, therefore, the tuning could likely be adjusted to offer a more aggressive error reduction. For $k = 0$ to 1.3 and 1.4 mm the response overshoots the set point and exhibits a decaying oscillation, which is indicative of an overly aggressive controller and is marginally stable. Notably, for $k = 0$ to 1.2 mm, the response of the controlled disturbance quickly reaches the zero level and does not oscillate, indicative of a properly tuned control system. This best-case tuning of the controller for this mid-range roughness-element height, and non-optimal tuning for the other values of k, indicates a subtle nonlinearity in the boundary layer response that is not captured in the linear plasma actuator model used here. The corresponding settling time, t_s, for each controlled disturbance to reach and maintain $\leqslant 10\%$ of the uncontrolled steady-state disturbance level is provided in the figure 15 inset axis; where $t_s = 0$ is the time when the feedback signal first exceeds 10 % of the uncontrolled level. The response of $k = 0$ to 1.2 mm provides the fastest settling time, while the other control response incur a longer settling time.

Another feature of these results is that the controlled cases all remain at a zero disturbance level for approximately 0.05 s longer than the uncontrolled results, before undergoing a sharp increase in the shear-stress disturbance at approximately $t = 0.21$ s. The slope of the controlled disturbance approximately matches that of the uncontrolled disturbance for some time ($0.21 \lesssim t \lesssim 0.29$ s) after rising above zero. The $k = 0$ to 1.4 mm result exhibits a similar response as the other k results, except that a very steep disturbance growth is experienced from $0.29 \lesssim t \lesssim 0.33$ s, and the controlled disturbance reaches the uncontrolled peak disturbance magnitude. As noted in figure 15, the feedforward (*ff*) controller output begins to take effect at $t = 0.106$ s (which is before the disturbance reaches the feedback sensor, i.e. purely feedforward control). Although the feedforward controller has an immediate effect in controlling the disturbance, the disturbance amplitude is not well predicted by this part of the model, resulting in the remaining disturbance level increase at $t = 0.21$ s (this point is further discussed in § 6).

Figure 16 summarizes the results of uncontrolled and controlled disturbances at the upstream and downstream shear-stress sensors at steady state. The downstream sensor, which captures the effectiveness of the control, demonstrates that the appropriate level of plasma voltage was supplied and the controlled disturbance shear stress, $\tau'_{d,\mathscr{C}}$, is driven to zero for all roughness-element heights.

In addition to the single-point downstream feedback sensor, the effectiveness of the control system can be considered over the y–z plane; this was done 5 mm downstream of the feedback sensor, at $x = 305$ mm. The results were acquired during the full roughness element motion cycle and phase averaged; steady-state disturbance results are provided in figure 17. Note, in order to collect y–z planar results of the controlled disturbance using the four roving hot wires, a dedicated feedback sensor was fabricated, similar to the upstream sensor, and located at $(x_{fb}-x_k, y, z) = (300, 1.5, 2.5)$ mm. Figure 17(*a*) provides the controlled disturbance for $k = 1.2$ mm, and demonstrates the successful disturbance attenuation at the feedback sensor location; however, total planar disturbance cancellation is not achieved. Examining the planar disturbance results of figure 7, it is clear that at the downstream sensor plane the steady-state disturbance has experienced a spanwise shift of approximately 1 mm toward the negative z direction. Furthermore, in figure 8, the steady-state downstream disturbance from the plasma actuator is shown to be slightly shifted to the $+z$ side, and somewhat stronger on the $-z$ than $+z$ side. Even so, the shear-stress sensor is located within a portion of the negative disturbance,
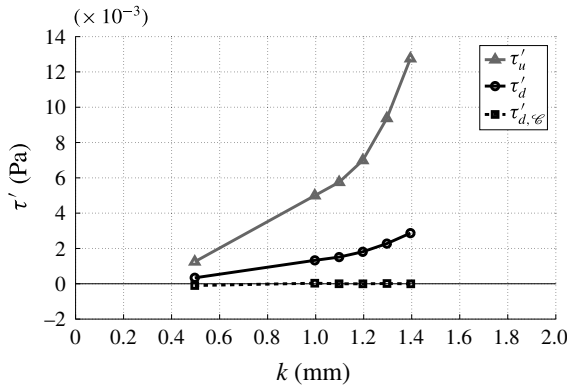
FIGURE 16. Steady-state control results for the upstream and downstream shear stress at various roughness-element heights with $U_\infty = 5.0$ m s^{-1} and the feedback sensor at $x-x_k = 300$ mm.
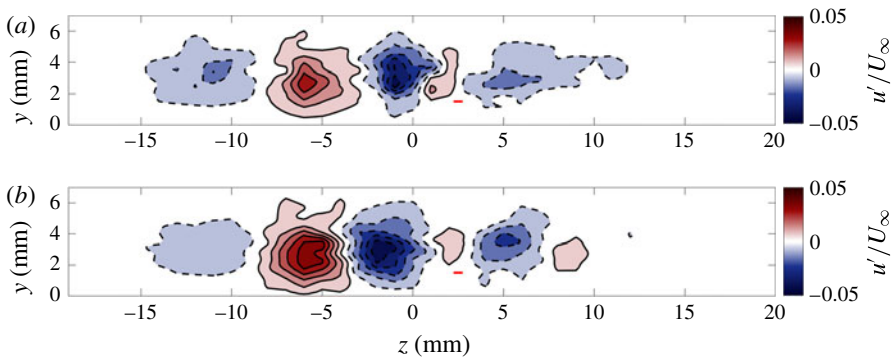

FIGURE 17. (Colour online) Steady-state streamwise velocity disturbance contours for the (a) downstream plane with control and $x-x_k = 305$ mm, $k = 1.2$ mm, and (b) downstream plane with a superposition of the $k = 1.2$ mm and $V = 2.4$ kV disturbances, $x-x_k = 305$ mm.

and the plasma actuator is therefore able to cancel the roughness-element-induced positive disturbance at the sensor location. The spanwise shift and slightly asymmetric disturbance prevents cancellation in the full downstream y–z plane.

The appropriate plasma actuator voltage for cancellation of the disturbance induced by the roughness element at $k = 1.2$ mm is $V \approx 2.43$ kV, according to the I/O control model. Therefore, the disturbances generated by the roughness element and plasma actuator in figures 7 and 8 are nearly matched at the downstream shear-sensor location of $(y, z) = (1.5, 2.5)$ mm; figure 17(b) demonstrates the superposition of these disturbances. The agreement between the controlled (figure 17a) and superposition (figure 17b) confirm that the roughness and actuator disturbances interact in a linear fashion. Furthermore, the agreement of the superposition and controlled disturbance results, indicates that with proper matching of the roughness element and plasma actuator disturbance strength and spatial shape, complete cancellation of the roughness-element disturbance in the y–z plane is expected. This matching can be achieved more easily in actual bypass transition, where the streaks are
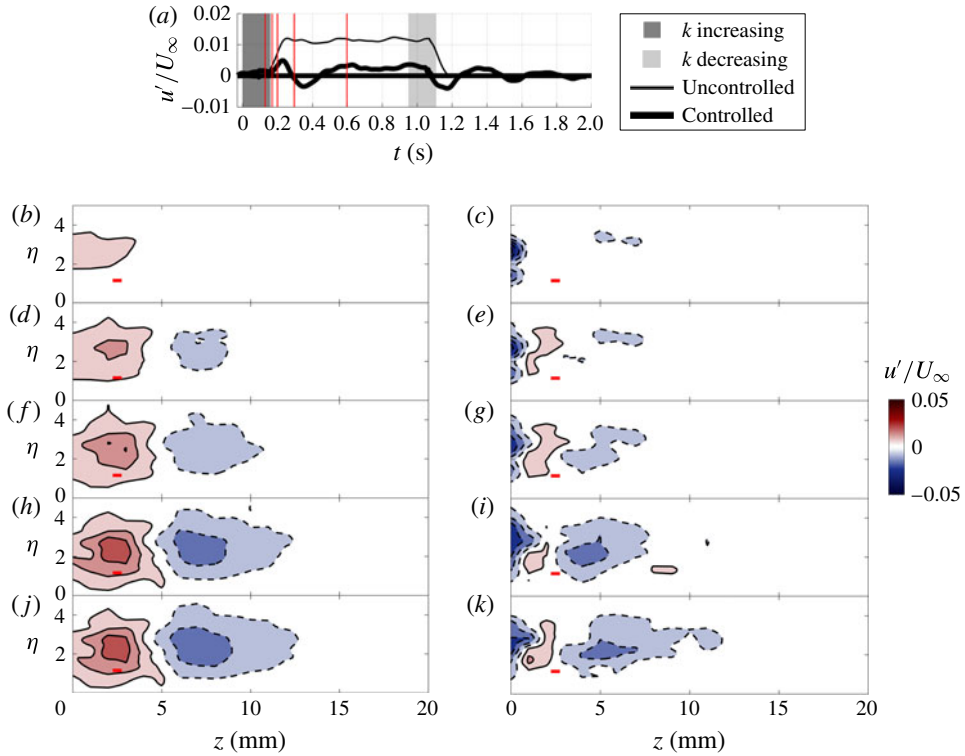
FIGURE 18. (Colour online) Temporal development of the uncontrolled (b,d,f,h,j) and controlled (c,e,g,i,k) unsteady disturbance in the $+z$ half-plane at $x-x_k = 305$ mm, with $k = 0$ to 1.2 mm, and the feedback sensor at $(x_{fb}-x_k, y, z) = (300, 1.5, 2.5)$ mm. Panel (a) provides the normalized velocity disturbance level versus time; the five disturbance contour results correspond to the five marked time instants at $t = 0.13$ s (b,c), 0.17 s (d,e), 0.20 s (f,g), 0.30 s (h,i), 0.60 s (j,k).

quasi-periodic, rather than localized along the spanwise direction. Specifically, by integrating multiple plasma actuators, each producing a disturbance with different fundamental wavenumber (e.g. one with the average streak spacing λ_z, a second with $\lambda_z/2$, a third with $\lambda_z/3$, etc), it would be possible to 'Fourier synthesize' a control disturbance with the same quasi-periodic signature as the streaks. Multiple rows of such actuators but shifted along the span would further enable adjustment of the spanwise phase of the disturbance to ensure that the control disturbance is out of phase with the streaks disturbance. This phase and magnitude of the control disturbance would be modulated in real time in response to data from a spanwise array of upstream feedforward sensors in order to adapt to random variation of natural streaks.

In addition to the steady-state results, the temporal evolution of the planar disturbance measurements in the $+z$ half-plane (containing the feedback sensor) is shown in figure 18 during the control cycle. The contours demonstrate the spatial distribution of the disturbance velocity over the y–z plane at $x-x_k = 305$ mm at five instants in time without (b,d,f,h,j) and with control (c,e,g,i,k). The maximum uncontrolled velocity disturbance, $u'(t)/U_\infty$, at the downstream shear-stress sensor is $\approx 1.2\%$, which is controlled to $\approx 0.2\%$.
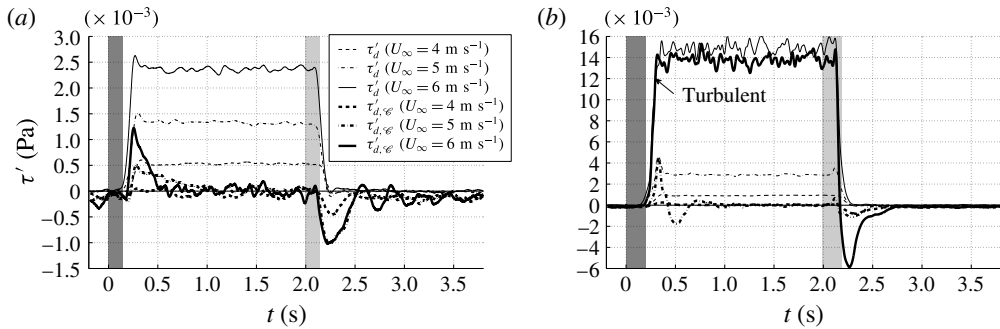
FIGURE 19. Unsteady control results for the downstream shear stress at various free stream velocities with the feedback sensor at $x_{fb}-x_k = 300$ mm and a roughness-element height of (a) $k = 0$ to 1.0 mm and (b) $k = 0$ to 1.4 mm. Uncontrolled- and controlled-flow cases are depicted using thin and thick lines respectively.

5.2. *Effect of free stream velocity*

The control model was developed for a free stream velocity of $U_\infty = 5.0$ m s^{-1}. In this section, the effectiveness of the controller at off-design conditions is investigated with a $\pm 20\,\%$ change in the free stream velocity, to $U_\infty = 4.0$ and 6.0 mm s^{-1}. Similar to changing the roughness-element height, altering the free stream velocity changes the disturbance strength. In addition, by altering the free stream velocity, the time delay characteristics of the boundary layer response will also change. The controller integral time constant, which is built into the feedback control system, is not adjusted to account for the altered convection time delay.

In figure 19(*a*), the uncontrolled and controlled responses at the downstream shear-stress sensor are provided for $k = 0$ to 1.0 mm. The controlled result for the on-design free stream velocity of $U_\infty = 5.0$ m s^{-1} demonstrates the largest response time to reach a zero disturbance level. For the higher free stream velocity of $U_\infty = 6.0$ m s^{-1}, the shorter convection time delay allows the feedback controller to more quickly integrate the controller error to reach the appropriate output control voltage. For the lower free stream velocity of $U_\infty = 4.0$ m s^{-1}, the controller is effective in driving the disturbance to zero without any delay. This is a surprising result given that none of the various roughness-element height results of figure 15 were sufficiently controlled to a zero disturbance level without feedback controller contribution, and the disturbances all exhibited a sharp increase as the roughness element was raised; followed by a slow control to zero. To explain this difference, the mechanism by which the plasma forces the flow should be further considered. As described by Hanson *et al.* (2014), the slower free stream velocity results in more momentum imparted to the air above the actuator (integrated force with respect to time). Thus, the fully controlled lower free stream velocity result of figure 19(*a*) is suspected to be due to a larger disturbance with $U_\infty = 4.0$ m s^{-1} (larger than the control model intends based on the I/O data at $U_\infty = 5.0$ m s^{-1}), which turns out to be well matched for complete control. This also explains why the $U_\infty = 6.0$ m s^{-1} results rises before the $U_\infty = 5.0$ m s^{-1} result. It was demonstrated in figure 15 that for all k, the rise in the controlled disturbance resulted after the upward motion of the roughness element occurred, and at nominally the same time delay from the start of the roughness motion; however, here, the disturbance with $U_\infty = 6.0$ m s^{-1} rises sooner, an indication that the feedforward controller is less effective due to a
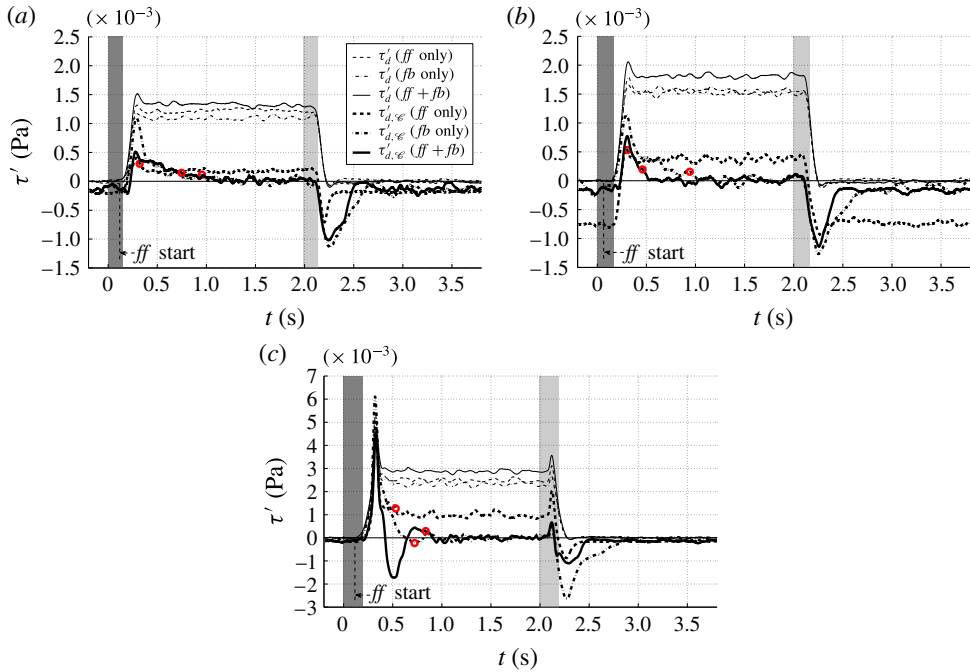
FIGURE 20. (Colour online) Unsteady control results for the downstream shear stress under feedforward only control (*ff*), feedback only control (*fb*), and feedforward + feedback control (*ff* + *fb*); with a roughness-element height of (*a*) $k = 0$ to 1.0 mm, (*b*) $k = 0$ to 1.2 mm, and (*c*) $k = 0$ to 1.4 mm and the feedback sensor at $x_{fb} - x_k = 300$ mm. Uncontrolled- and controlled-flow cases are depicted using thin and thick lines respectively. The settling time for each signal is noted with a ○ marker.

weakened actuator-induced disturbance. This discussion also holds true with the $k = 0$ to 1.4 mm results in figure 19(*b*).

In figure 19(*b*), the uncontrolled and controlled response at the downstream shear-stress sensor are provided with $k = 0$ to 1.4 mm, with the most notable result being the presence of turbulent fluctuations at the larger free stream velocity. As discussed previously, for the lower velocity, the controller can act more quickly, which in the present case removes the undershoot observed at the on-design velocity.

5.3. *Effect of control strategy*

The effectiveness of the feedforward, feedback and combined controllers were analysed for three roughness-element deployment heights, $k = 0$ to 1.0, 1.2 and 1.4 mm, and the results are provided in figure 20(*a–c*), respectively. In figure 20(*a*), the disturbance controlled using feedforward only demonstrates an immediate disturbance reduction. However, the feedforward gain is not perfectly tuned and the controlled disturbance amplitude remains above zero (at 17 % of the uncontrolled case) during the steady disturbance time period ($0.6 \lesssim t \lesssim 2.0$ s). The feedback only controlled disturbance reaches a zero disturbance level, but the time required to do so is relatively large. Furthermore, the initial disturbance level nearly reaches the full uncontrolled level which could initiate transition if k is sufficiently high. The combined feedforward and feedback control shows that the controlled disturbance is

reduced immediately and over all times, reaching a zero disturbance level slightly faster than the purely feedback control result. The benefit of the feedforward control is clearly the fast reduction of the disturbance level, which is significant in this case where there is an initial large disturbance overshoot, while the feedback control allows the controller output to be adjusted to achieve a zero disturbance level.

The response with $k = 0$ to 1.2 mm, in figure 20(b), demonstrates many of the same characteristics as that with the previous case; however there are a few notable details. The feedforward only response shows the undisturbed shear stress when $k = 0$ as less than zero. It was determined, by examining a record of the controller output, that the controller was sporadically turning the plasma on/off when the roughness element was withdrawn for this control case and therefore providing a low level forcing, resulting in a negative disturbance. This was linked to deviation in the feedforward sensor output level from Blasius in this case; perhaps due to slight sensor drift. This issue does not affect the response of the controller during the roughness-element disturbed portion of the time series. Figure 20(b) shows: (i) the very fast, but incomplete control supplied by feedforward only controller, (ii) the slow, but complete control by feedback only controller and (iii) the fast and complete control of the combined controller.

In figure 20(c), the feedforward only response shows a reduced, but still non-zero, disturbance amplitude with control. However, unlike the lower roughness-element height results, the feedforward+feedback result exhibits an oscillatory response resulting in a prolonged settling time. This is due to the strong positive overshoot which causes the feedforward controller to maximize its output. The disturbance remains very strong even with feedforward control, therefore, the feedback controller reaches a very large voltage contribution as well, resulting in a negative disturbance that persists after the spike in positive disturbance quickly relaxes to the steady-state level. The feedback only result exhibits a very small overshoot, and as a result, reaches a zero disturbance level the fastest.

5.4. *Effect of the streamwise location of the feedback sensor*

In an effort to assess some aspects of the streamwise sensor placement, a set of control experiments was performed with the downstream shear-stress sensor positioned at various locations: $x_{fb} - x_k = 125$, 200 and 300 mm. The wall-normal and spanwise position of the sensor was not changed, since the spatial distribution of the disturbance does not change significantly over this streamwise domain (see Bade 2014). Experiments were carried out for $k = 0$ to 1.0, 1.2 and 1.4 mm; however, the results at each k were equivalent, thus, only the $k = 0$ to 1.2 mm results are presented.

As shown in figure 21, locating the feedback sensor further upstream toward the actuator results in a shorter convective time delay and settling time. Furthermore, the feedback gain, K_{fb} for the more upstream sensor locations was larger, resulting in a more aggressive but still stable controller. An assessment of the settling time for all k values is provided in figure 21(b). For all k, the $x_{fb} - x_k = 200$ mm results reach the fully controlled zero disturbance level faster than the $x_{fb} - x_k = 300$ mm, demonstrating that positioning the downstream sensor closer to the actuator benefits the system response time and would ultimately allow control of higher-frequency disturbances, as would be expected. Additionally, the $x_{fb} - x_k = 125$ mm result for $k = 0$ to 1.2 mm has the smallest settling time. The control results recovered a zero disturbance level faster with $k = 0$ to 1.2 mm than for $k = 0$ to 1.0 mm and 0 to 1.4 mm. This is consistent with the results in § 5.1, which found that the controller was tuned most
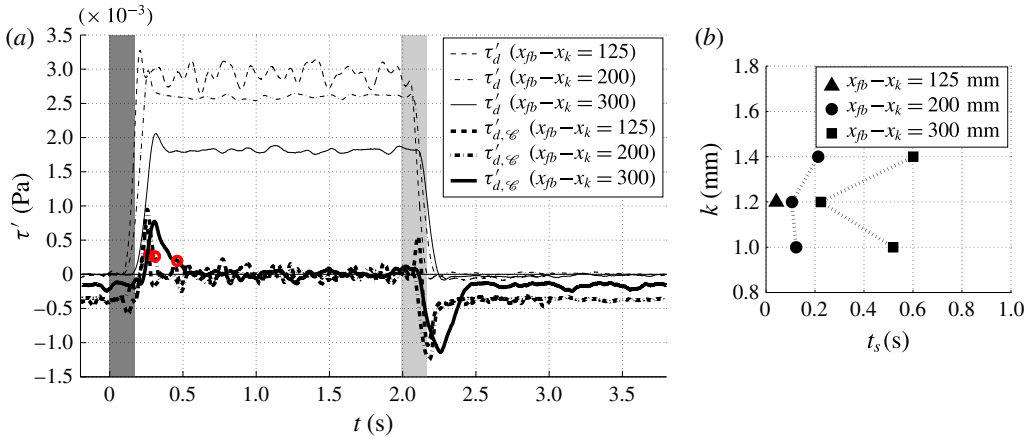
FIGURE 21. (Colour online) Unsteady control results for the downstream shear stress with the feedback sensor at multiple downstream locations (in mm) with a roughness-element height of $k = 0$ to 1.2 mm for the full cycle time; the settling time for each signal is noted with a ∘ marker. The inset provides the settling time for each controlled disturbance. Uncontrolled- and controlled-flow cases are depicted using thin and thick lines respectively.

appropriately to quickly attenuate the disturbance generated when $k = 0$ to 1.2 mm. Also, it is observed that as the feedback sensor is located further upstream, the performance of the controller is less sensitive to changes in the roughness-element height.

5.5. *Control bandwidth*

The frequency response of the control model was investigated by varying the motion parameters of the roughness element with $k = 1.0$ to 1.2 mm. Although a sinusoidal motion would be ideal, the software operating the Squiggle motor was not amenable; therefore, a sinusoidal motion was approximated by a fine trapezoidal pattern with varying hold times, t_h, such that an oscillatory motion was adequately produced as shown in figure 22(*a*), within the velocity and acceleration limits previously discussed. Alternatively, each roughness element motion may be divided by the period of motion, T_k, resulting in a normalized time scale and an associated characteristic frequency of oscillation, $f_k = 1/T_k$, rather than a characteristic hold time (see figure 22*b*). Thus, by prescribing various t_h values, a range of frequencies, f_k, was achieved.

Figure 23 shows the uncontrolled and controlled disturbance for different roughness-element motion frequencies. At a frequency of $f_k = 2.00$ Hz, a zero disturbance is achieved with control, but at larger f_k values a zero disturbance does not appear to be reached. A mean-removed fast Fourier transform (FFT) of each uncontrolled and controlled disturbance signal was performed to analyse the disturbance energy contained at the fundamental frequency of each unsteady disturbance (i.e. at the roughness-element oscillation frequency). The FFT results are presented to the right of each signal plot in figure 23 and demonstrate that the cycle frequency, f_k, was the strongest component. Futhermore, figure 23 shows that the mean and maximum disturbance levels are successfully reduced at all f_k.

To quantify these observations, maximum (MAX), mean and r.m.s. values are calculated for the uncontrolled and controlled disturbance traces shown in figure 23,
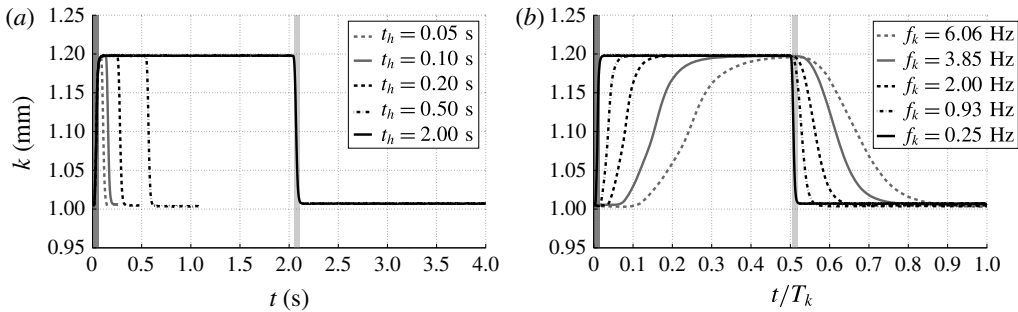
FIGURE 22. Unsteady roughness-element motion from $k = 1.0$ to 1.2 mm with (*a*) various steady-state hold times, t_h, resulting in (*b*) a range of equivalent unsteady disturbance frequencies, $f_k = 1/T_k$. Grey bands demonstrate periods when the roughness element is in motion for the $t_h = 2.0$ s ($f_k = 0.25$ Hz) case.

and are presented in figure 24(*a*). The maximum disturbance experiences a significant reduction with control, which reduces the likelihood of the streak disturbance to experience transition. The mean disturbance is driven to nearly zero at all investigated frequencies. In figure 24(*a*), the control is more effective at reducing the r.m.s. of the lower frequencies, and the reduction diminishes with increased frequency. This effect may be seen more clearly on a magnitude frequency response plot, depicting the ratio of the controlled and uncontrolled peak FFT values of the downstream shear-stress disturbance versus frequency, as in figure 24(*b*). A cutoff frequency where the control reduces the shear-stress fluctuations by more than 3 dB, or 71 %, of the uncontrolled disturbance FFT peak is identified at 1.3 Hz.

6. Modelling and discussion

As seen in figures 10 and 12, the response of the boundary layer (plant) to the disturbance and actuation input can be accurately modelled using simple zeroth- and first-order systems with a time delay, (4.1) and (4.4). Thus, it is straightforward to simulate the controlled system response and explore the control effectiveness from a perspective that is broader than that learned from only the experimental data. In particular, as found in §5.5, where $x_{fb} - x_k = 300$ mm, the control system bandwidth is of the order of 1–2 Hz. Though this bandwidth can be improved by moving the feedback sensor closer to the actuator (hence reducing the convective time delay, t_V), this result demands further scrutiny because: (i) ideally, the feedforward controller should be 'infinitely' fast, independent of x_{fb} (so the reason for this very limited bandwidth is not clear); (ii) a bandwidth of a few Hz will not be useful for practical applications (e.g. controlling transition beneath a turbulent free stream), and therefore it is desirable to project to what extent is it possible to improve the response speed of the control system relative to what is found in the present experiments.

Referring to figure 9, the transfer functions for the feedforward (*ff*), feedback (*fb*) and combined (*ff* + *fb*) controlled systems may be written, respectively, as

$$G_d^{ff} = G_d + FP, \tag{6.1}$$

$$G_d^{fb} = \frac{G_d}{1 + CP}, \tag{6.2}$$
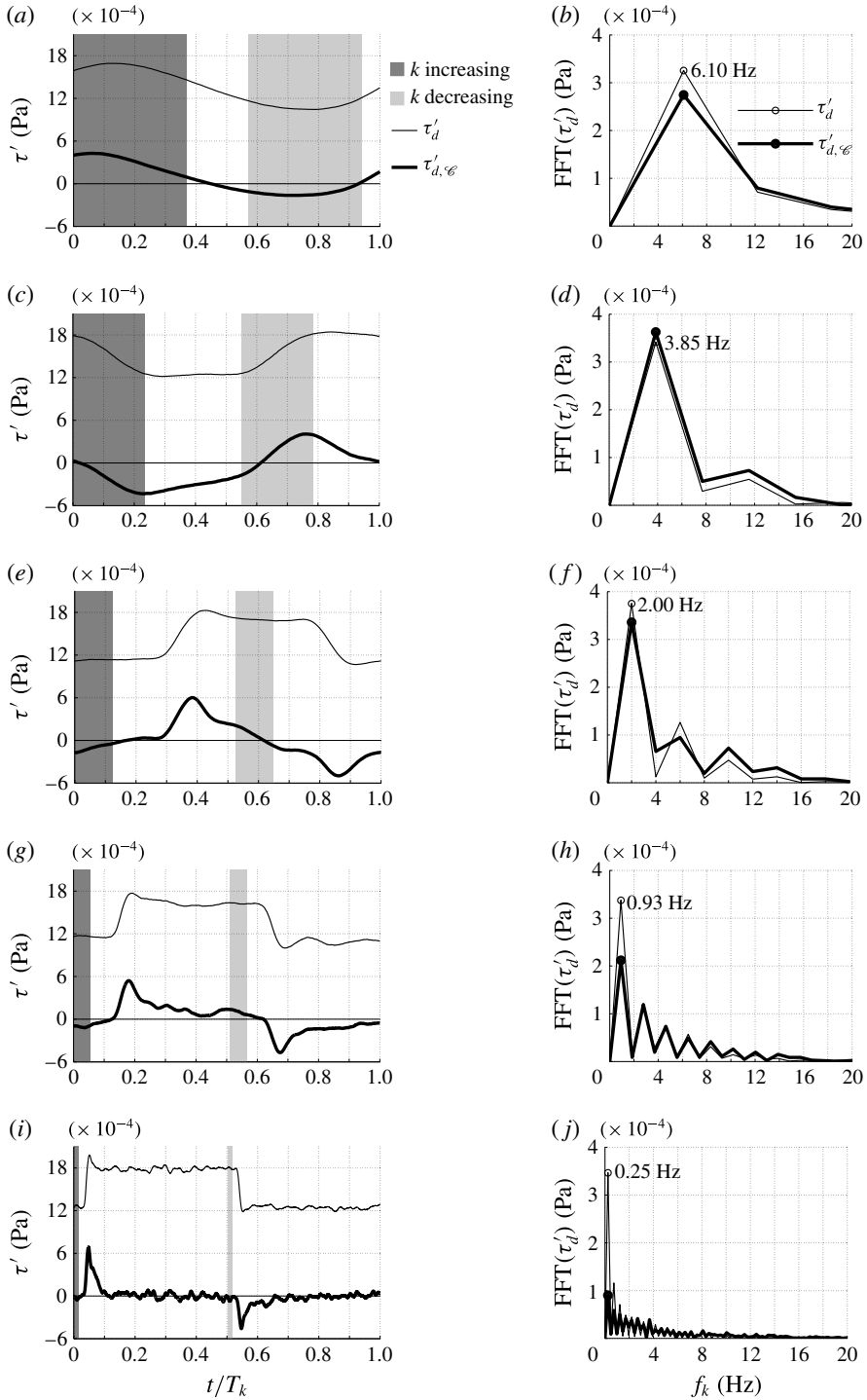
$$G_d^{ff+fb} = \frac{G_d + FP}{1 + CP}. \tag{6.3}$$

FIGURE 23. Unsteady roughness-element motion from $k = 1.0$ to 1.2 mm with various frequencies, f_k (6.06 Hz (*a,b*), 3.85 Hz (*c,d*), 2.00 Hz (*e,f*), 0.93 Hz (*g,h*), 0.25 Hz (*i,j*)): phase-averaged uncontrolled and controlled signals (*a,c,e,g,i*) and the corresponding FFT (*b,d,f,h,j*).
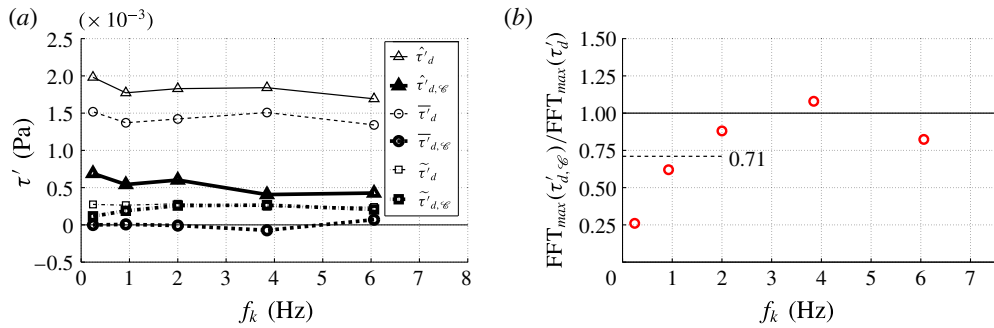
FIGURE 24. (Colour online) For various roughness-element disturbance frequencies with $k = 1.0$ to 1.2 mm the (*a*) maximum, $\hat{\tau}'_d$, mean, $\overline{\tau'_d}$ and r.m.s., $\tilde{\tau}'_d$, of the uncontrolled and controlled disturbance periods, and (*b*) the ratio of the controlled to the uncontrolled disturbance peak FFT values.

The above transfer functions are used to simulate the output (controlled) downstream wall-shear stress for *ff*, *fb*, and *ff* + *fb* control using the upstream shear-stress disturbance measured during experiments. This is done for the $k = 0$ to 1.2 mm case; the experimental results for which are depicted in figure 20(*b*).

Before examining the comparison of the model and experimental results, it should be noted that in the case of *ff* control, it is necessary to decompose τ'_u into two parts in order to account for a peculiarity of this case. Consider figure 20(*b*), where it is seen that during periods when the boundary layer is undisturbed, τ'_u has an unexpected tangible negative deviation from zero. This deviation is found to be linked to an occasional small 'drift' in the upstream sensor output above the Blasius level, notwithstanding that no streaks are present in the boundary layer (this may be seen in the average τ'_u signal, given by the solid line in figure 25). Thus, to compute τ'_d in the case of *ff* control, the measured τ'_u signal is offset and scaled to produce zero disturbance when the roughness element is withdrawn while maintaining the same disturbance steady-state level when the element is deployed; see figure 25. This offset-and-scaled signal is used in conjunction with (6.1) to compute one component of the output. The other component of the output is computed from a deviatoric input comprising the difference between the full τ'_u and the offset-and-scaled signal. As seen from figure 25, the deviatoric τ'_u component captures the non-zero τ'_u level when the roughness element is withdrawn and vanishes when the element is deployed. This deviatoric signal is used as an input to only the second term in (6.1) to compute the second component of the output. This output is then superposed on the output from the offset-and-scaled signal to produce the complete model output for *ff* control.

Figure 26 depicts the modelled and measured control output for the *ff*, *fb* and *ff* + *fb* control cases; the model reasonably represents the response of the physical system. Though not exact, the response time of the physical and modelled system is similar. Therefore, it is sensible to use the model to explore the control system characteristics. A quantity that is of particular interest is the 'disturbance shear-stress attenuation', defined here as the ratio A of the controlled and uncontrolled shear-stress amplitude ($|\tau'_{d,c}|$ and $|\tau'_d|$, respectively) for sinusoidal input disturbance τ'_u. The dependence of A on frequency is given in figure 27 for the three cases considered in figure 26. Clearly, it is desirable to maintain a large negative dB value of A over as wide of a frequency range as possible. For comparison purposes, the point of -3 dB (dotted line in
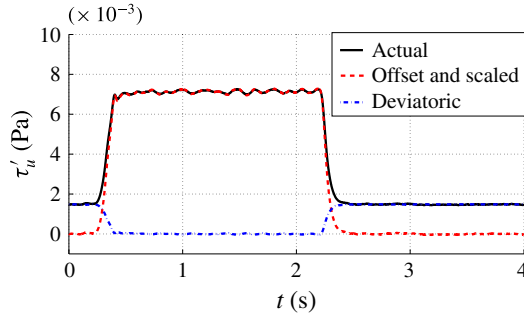
FIGURE 25. (Colour online) Illustration of the decomposition of the upstream wall-shear-stress signal (solid line) into an offset-and-scaled (dash line) and deviatoric (dash-dot line) components for modelling of the *ff* control case.
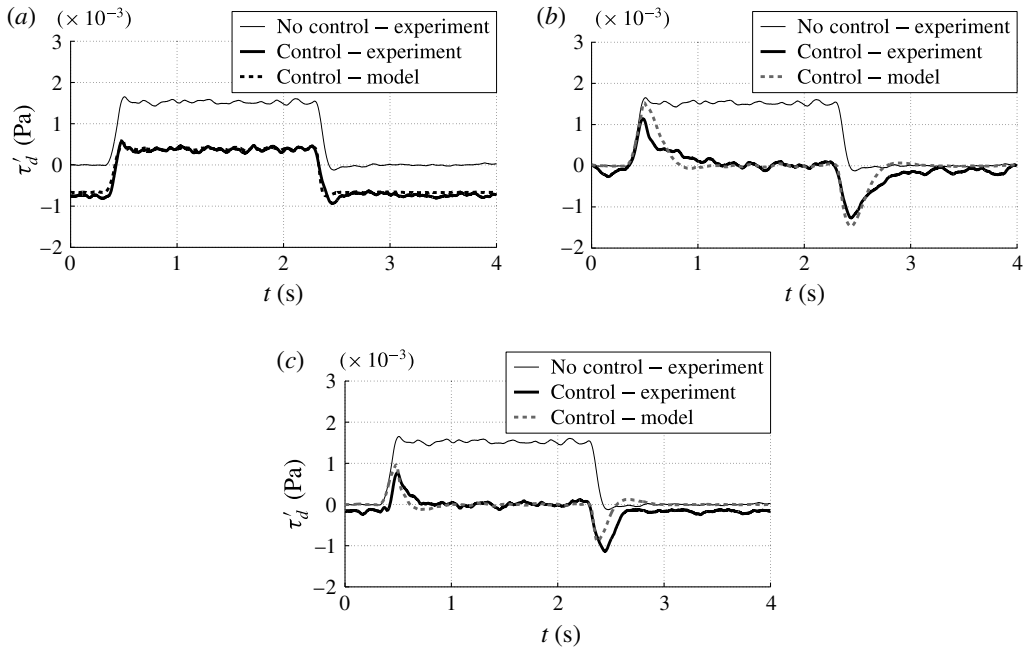

FIGURE 26. Comparison between experimental and modelled τ_d' evolution without and with control using (*a*) *ff*, (*b*) *fb* and (*c*) *ff + fb* control methods.

figure 27) is selected as a minimum desirable attenuation. Figure 27 shows that the combined *ff + fb* control system is able to attenuate τ_d' amplitude below the -3 dB point for frequencies less than 1–2 Hz, consistent with the experimental results in figure 24. The *fb* system has a useful bandwidth of only 0.5 Hz and the *ff* system bandwidth is limited to below 3–4 Hz. As discussed previously, the latter finding is particularly surprising given that the ideal *ff* system bandwidth should be infinite. Therefore, it is important to understand what factors could cause such a severe deterioration in response of the *ff* system with practical implementation.

The effectiveness of the *ff* system relies on having accurate models of the boundary layer response to both the disturbance and the actuation. Given that the form of the
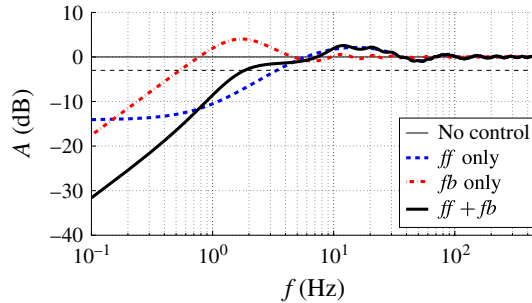
FIGURE 27. (Colour online) Frequency dependence of τ_d' attenuation ratio A for the ff, fb and $ff + fb$ controllers. A dashed line is provided at -3 dB for reference.

models used here represent the boundary layer response well (figures 10 and 12), in the following discussion, an examination is carried out on the effect of the accuracy of determining the model parameters on the control system limitations. Additionally, given the very slow nature of the implemented feedback system with $x_{fb}-x_k = 300$ mm, the control effectiveness will also be examined for three values of the x_{fb}, by shortening the convective time delay (t_V) from 0.1 s (of the same order as for $x_{fb}-x_k = 300$ mm) to 0.01 s and 0.001 s. The last value would place the sensor within a fraction of a mm downstream of the actuator, which is likely not feasible in practice, but is representative of the limiting improvement of the feedback system response by changing the feedback sensor position.

Considering (4.7), the ideal ff controller is constructed based on three parameters: the disturbance gain K_τ, the actuation time constant t_c and the differential convective time delay (hereafter referred to as DCTD $= t_\tau - t_V$, see (4.7)). In this exploration, the value of only one ff controller parameter is varied while other parameters are kept at their ideal values. The ff controller transfer function employed is that given by the ideal form (4.7), rather than the simplified form (4.8) employed in the experiments. Also, the following plant parameters were used, which are approximately the same as those in the experiments: $K_\tau = 0.2$, $t_\tau = 0.1$ s, $t_V = 0.1$, 0.01, and 0.001 s and $t_c = 0.025$ s. Note that variation of t_V implicitly results in a change of the feedback gain since computation of the latter utilizes t_V (4.11). Thus, the effect of the feedback gain is also examined in the following section.

6.1. *Effect of the controller gain*

The feedforward controller gain was determined from the I/O model relating the upstream wall-shear-stress disturbance to its downstream counterpart; i.e. K_τ. However, the employed ff controller gain only results in complete cancellation of τ_d' for those individual streaks which happen to produce a ratio τ_u'/τ_d' equivalent to that obtained from the phase-averaged response. In practice, the streaks exhibit small cycle-to-cycle variation and therefore imperfect cancellation was generally observed. Deviation from this average value is expected, which is true not only in the current model problem but also in the more relevant practical problem involving stochastic streak formation beneath a turbulent free stream. This concept is exemplified in figure 28 for a unit step change in τ_u', where the controller gain is 20 % smaller than the actual K_τ. The figure also depicts the fb and $ff + fb$ system responses. The responses are qualitatively consistent with those observed experimentally (figure 20), with the exception of the
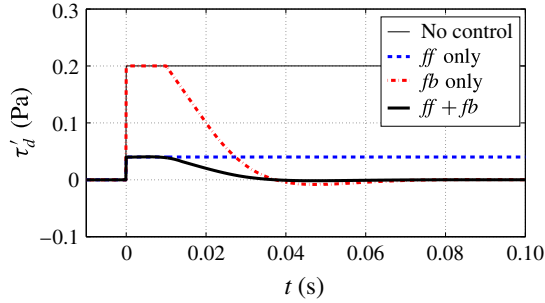
FIGURE 28. (Colour online) Evolution of τ_d' in response to unit step change in τ_u' when the *ff* controller gain is 20 % off it's ideal value ($t_V = 0.01$ s); showing the uncontrolled and controlled responses.
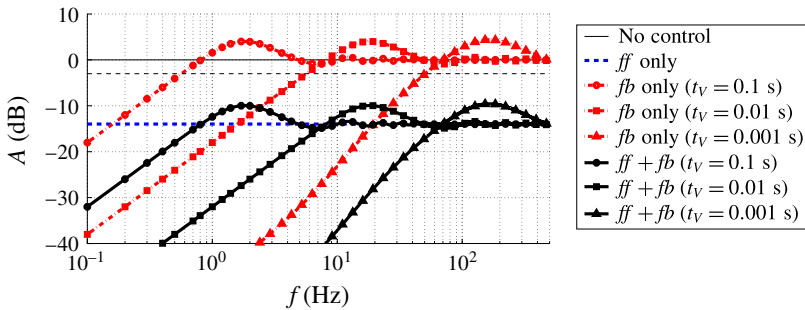

FIGURE 29. (Colour online) Frequency dependence of τ_d' attenuation ratio A for the *ff*, *fb* and *ff* + *fb* controllers when the *ff* controller gain is 20 % off it's ideal value: uncontrolled and controlled response for $t_V = 0.1$, 0.01 and 0.001 s. A dashed line is provided at -3 dB for reference.

abrupt ('infinitely fast') response of the *ff* system shown in figure 28 (a reflection of the ideal nature of the modelled *ff* controller). Overall, figure 28 shows that the *ff* system is extremely fast, yet it is unable to cancel τ_d' completely given the 20 % 'error' in the controller gain. The incorporation of the feedback in the combined *ff* + *fb* controller corrects for the remaining error, albeit at a slower time scale.

The results in figure 28 demonstrate that a non-ideal *ff* controller gain should cause a deterioration in τ_d' attenuation A but not in the speed of response of the system. This is exemplified more clearly in plots of A versus frequency in figure 29, for the three different placements of the feedback sensor. For all cases, the frequency response of A is flat and has a value of -13.98 dB. Thus, the *ff* controller's bandwidth is infinite, although the magnitude of A deteriorates from $-\infty$ (for the theoretical case) to approximately -14 dB. This shows that knowledge of the correct controller gain with high accuracy is not critical to the performance of the *ff* system. This is particularly true when combined with the *fb* system, which as seen from figure 29, is capable of enhancing A beyond the *ff* system's capability, within the bandwidth of the *fb* system. The latter is seen to improve by two orders of magnitude from approximately 0.5 to 50 Hz by moving the feedback sensor upstream (i.e. by decreasing t_V).
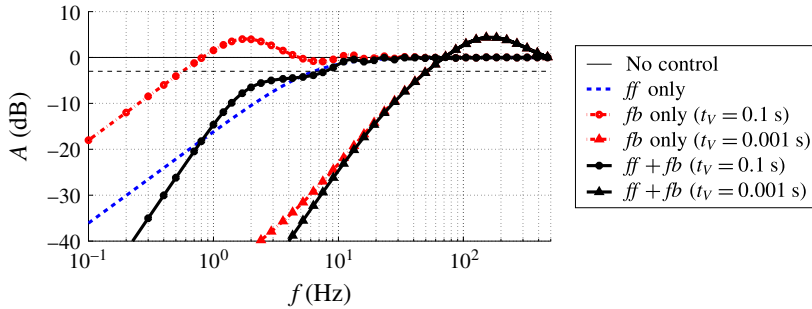
FIGURE 30. (Colour online) Frequency dependence of τ_d' attenuation ratio A for the *ff*, *fb* and *ff* + *fb* controllers when the actuation time constant t_c is not taken into account in the *ff* controller model: uncontrolled and controlled response for $t_V = 0.1$ and 0.001 s. A dashed line is provided at -3 dB for reference.

6.2. *Effect of the actuator time constant*

In the experimental demonstration, the actuation time constant t_c was ignored in constructing the *ff* controller model, for simplicity. The simulated frequency response of A with $t_c = 0$ is shown in figure 30 for two feedback actuator placements, corresponding to *fb* system bandwidths of approximately 0.5 and 50 Hz. Considering the former of these two cases, which is similar to the current experimental implementation for x_{fb}–$x_k = 300$ mm, it is shown that neglecting t_c greatly reduces the *ff* controller bandwidth. Specifically, unlike the 'infinite' bandwidth maintained by the *ff* controller even in the presence of imperfect controller gain, neglecting t_c reduces the bandwidth to approximately 6 Hz. Using (4.7), it is straightforward to show that if all other controller parameters are perfect, ignoring t_c results in an *ff* controller that is effectively a first-order high-pass filter with a time constant of t_c (cutoff frequency of 6.3662 Hz for the t_c value of 0.025 s used here).

It is also noteworthy that given the slow *fb* system response in figure 30 where $t_V = 0.1$ s, the combined *ff* + *fb* possesses a bandwidth that is essentially no different from the *ff* system alone. On the other hand, when the *fb* system is substantially faster (figure 30 where $t_V = 0.001$ s), the response is dictated by the *fb* system response alone, and combining the *ff* and *fb* system provides no additional value. However, if the t_c is accounted for, even if underestimated by 50 % (see figure 31), not only substantial attenuation is retained by the *ff* system at high frequencies, but also when the *fb* system is fast, the combined *ff* + *fb* system could outperform the *fb* only system. Therefore, in practice, it is important to account for t_c when constructing the *ff* controller; although the value of t_c need not be known with high accuracy for effective control.

6.3. *Effect of the differential convective time delay (DCTD)*

Another simplification made in the present experimental implementation of the *ff* controller is to set the time delay of the controller, resulting from the difference between the convective time delay of the roughness and the actuator disturbances, DCTD, to zero. This is done for two reasons: (i) the DCTD was approximately only one-tenth of each of the measured convective time delays and (ii) though
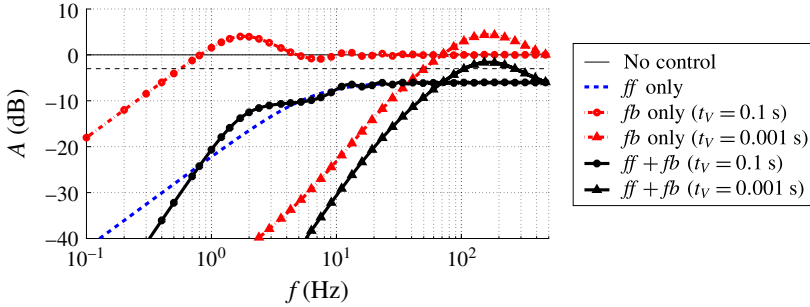
FIGURE 31. (Colour online) Frequency dependence of τ_d' attenuation ratio A for the ff, fb and $ff + fb$ controllers when the actuation time constant t_c used in constructing the ff controller is 50 % off the perfect value: uncontrolled and controlled response for $t_V = 0.1$ and 0.001 s. A dashed line is provided at -3 dB for reference.

counter-intuitive, t_τ is found to be smaller than t_V (a discussion of this is given at the end of this section), and hence a non-causal ff controller would be required to account for the DCTD, which is impossible to implement in practice.

Figure 32 displays the frequency response of A obtained when all ff controller parameters are perfect except for an underestimation of the DCTD by 0.02 s, which is 20 % of the value of t_τ. It is immediately evident from figure 32 that the inaccuracy of the DCTD value used in constructing the ff controller results in a severely reduced ff controller bandwidth to approximately 5–6 Hz. In addition, the dependence of A on frequency is such that it has a lobed shape where not only attenuation but also amplification ($A > 0$ dB) of τ_d' is possible. This behaviour, which is sustained over all frequencies, is easy to understand physically. Specifically, when the error in DCTD (e_{DCTD}) is non-zero, the control disturbance arrives at the control plane e_{DCTD} seconds later than the roughness-induced disturbance. For certain disturbance frequencies, the delay will be such that the two sinusoidal disturbances destructively interfere, as desired; while for other frequencies, the disturbances will constructively interfere, doubling the amplitude (corresponding to 6.02 dB). The frequencies at which the constructive interference takes place is given by

$$2\pi f_n e_{DCTD} = (2n + 1)\pi; \quad n = 0, 1, \ldots, \tag{6.4}$$

where f_n is the frequency of oscillation of the disturbance. For the present case of $e_{DCTD} = 0.02$ s, the first frequency is $f_1 = 25$ Hz. As the e_{DCTD} increases, this frequency becomes lower, limiting the bandwidth even further and *vice versa*. It is interesting that this limiting frequency is only dependent on e_{DCTD} and not the individual convective time delays. Therefore, it is very important to know the convective time delays with very good absolute accuracy, regardless if they are large or small. For example, an error of 1 ms in the DCTD would correspond to a limiting frequency of 500 Hz, and a bandwidth of the ff controller well below that.

Not knowing the DCTD with high accuracy limits the effectiveness of the ff controller substantially, relative to its theoretical performance. This is particularly the case for applications involving boundary layer transition beneath a turbulent free stream where the streaks and their characteristics, including convection speed, are stochastic. In this case, unless there is a way to adapt the ff controller in real time to the variation of the convective time delay, the performance of the ff controller would
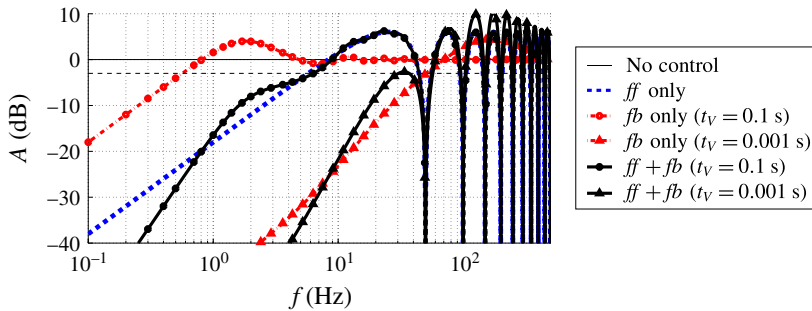
FIGURE 32. (Colour online) Frequency dependence of τ'_d attenuation ratio A for the ff, fb and $ff + fb$ controllers when the ff controller's time delay (DCTD) is off by 0.02 s: uncontrolled and controlled response $t_V = 0.1$ and 0.001 s. A dashed line is provided at -3 dB for reference.

vary from one streak to another with both streak stabilization and destabilization possible. Perhaps in such a case, the optimal DCTD is the one corresponding to some statistical average where, on balance, the effect of the stabilized streaks outweighs that of the destabilized ones. This is in agreement with the work of Lundell (2007), who employed ff only control of the boundary layer beneath a turbulent free stream using wall shear sensors similar to those used here in conjunction with suction-hole actuators. Lundell found that at a given free stream velocity, there exists an optimal time delay between the sensor and the actuator (i.e. the controller time delay) which produces the best control effect.

The sensitivity of the ff controller performance to the variation of the convective time delay of the boundary layer streaks and the control disturbance underlines the added benefit of having a concurrent fb system. At its fastest response speed (figure 32 where $t_V = 0.001$ s), the $ff + fb$ system has a bandwidth of approximately 50 Hz, similar to the fb system. This exemplifies a case where the DCTD error is fairly large, yielding an ff system bandwidth of only a few Hz. However, the presence of feedback guarantees that the control bandwidth will not drop below that of the fb system. Thus, in a stochastic environment, for those streaks where the actual DCTD matches the controller DCTD, the presence of the ff system should produce a control with good bandwidth. For other streaks, the presence of the fb system guarantees a minimum bandwidth that can be optimized by locating the feedback sensor as close as practically possible to the actuator.

Another point related to DCTD that is of practical importance concerns the situation arising in the present experimental implementation where t_V is found to be larger than t_τ, making it impossible to match the physical and ff controller DCTD. This issue can be linked to the use of fourth-order Butterworth filters to low-pass filter both τ'_u and τ'_d below 20 Hz. The use of this filter, which was done to remove noise, does not affect the measurement of t_τ since both the input (τ'_u) and output (τ'_d) are equally filtered. On the other hand, when measuring t_V, only the output (τ'_d) is filtered. Figure 33 shows the modelled unit step response of the boundary layer for actuation input with/without the Butterworth filter. As seen from the figure, the response of the system with the filter is effectively the same as without the filter but with an added time delay. This delay explains the counter-intuitive data showing t_V to be larger than t_τ. More significantly, this discussion shows that, depending on the filter characteristics, filtering the feedforward and feedback signals could introduce
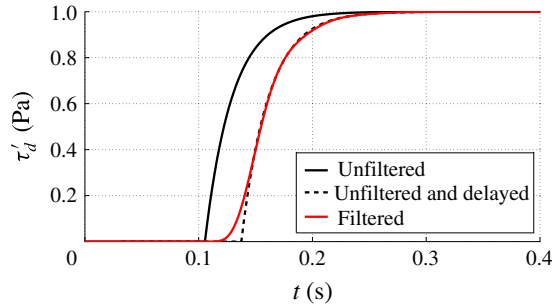
FIGURE 33. (Colour online) Demonstration of the effective time delay introduced into the measured downstream shear stress because of the use of fourth-order Butterworth low-pass filter.

time delays that cannot be corrected for in the *ff* controller design (since it would require non-causal implementation of the controller); hence, substantially limiting the performance of the *ff* controller. If such filters are necessary, a possible remedy is to move the upstream sensor further upstream to increase t_τ (i.e. detect the *ff* signal earlier) by a sufficient amount to offset the actuation delay provided by the filter.

7. Conclusions

This investigation reports on an experimental implementation of a feedforward–feedback control system for eliminating/weakening linear streaks in a Blasius boundary layer; toward the greater goal of controlling bypass transition. A canonical arrangement was considered where streaks were introduced in a systematic and tractable method using an isolated and unsteady roughness element. The boundary layer disturbances were successfully controlled by a plasma actuator that produced streaks of an opposite sense. The input to the controller was obtained from an upstream (feedforward) and a downstream (feedback) wall-shear-stress sensor with the objective of driving the disturbance at the feedback sensor to zero. Design of the feedforward and feedback controllers was based on input/output models of the measured boundary layer response to forcing by the roughness element and plasma actuators. It was found that zeroth- and first-order system models, with time delay, accurately capture the boundary layer response. Concurrent evaluation of the control system though experiments and system models provided improved analysis, and a boarder perspective.

The experimental results demonstrate the practical feasibility to implement the control methodology. In particular, as implemented, the control was effective over a range of roughness-element heights (disturbance strengths) and feedback sensor locations. The feedforward control provided fast, albeit incomplete, control of the disturbances, while the feedback control ensured control to the target set point, but at a relatively slow time scale. In addition, the system was robust to variation in the free stream velocity that deviate from the conditions at which the input/output models were obtained. However, the overall bandwidth of the system was limited to 1–2 Hz. Using a model of the control system it is shown that the bandwidth of the controller may be improved by one to two orders of magnitude by moving the feedback sensor closer to the actuator; a finding that agrees with the experimental observations. Further improvements in the bandwidth are also possible by improving

the feedforward model. A particularly critical parameter for the effectiveness of the feedforward controller is the difference in the convective time of the 'naturally' occurring disturbance as it travels from the upstream to the downstream sensor, and the convective time of the actuator disturbance to reach the downstream sensor. If not known with high accuracy, this parameter leads to substantial deterioration in the bandwidth of the feedforward control. An important ramification is when applying the control to bypass transition beneath a turbulent free stream where the convective time scales exhibit stochastic variation, making it impossible for the feedforward control to be effective for controlling all streaks. However, the coexistence of the feedback control ensures 'minimum guaranteed bandwidth' for controlling streaks for which the feedforward control is not effective. Future work should focus on assessing the effectiveness of the control beneath a turbulent free stream.

Acknowledgements

REFERENCES

ANDERSSON, P., BRANDT, L., BOTTARO, A. & HENNINGSON, D. 2001 On the breakdown of boundary layer streaks. *J. Fluid Mech.* **455**, 289–314.

ASAI, M., MINAGAWA, M. & NISHIOKA, M. 2002 The instability and breakdown of a near-wall low-speed streak. *J. Fluid Mech.* **455**, 289–314.

ASTROM, K. J. & MURRAY, R. M. 2010 *Feedback Systems*, chap. 10.4, pp. 306–308. Princeton University Press.

BADE, K. M. 2014 On the physics and control of streaks induced by an isolated roughness element. PhD thesis, Michigan State University.

BENARD, N. & MOREAU, E. 2014 Electric and mechanical characteristics of surface AC dielectric barrier discharge plasma actuators applied to airflow control. *Exp. Fluids* **55**, 1–43.

CATTAFESTA, L. N. & SHEPLAK, M. 2011 Actuators for active flow control. *Annu. Rev. Fluid Mech.* **43**, 247–272.

CORKE, T. C., POST, M. L. & ORLOV, D. M. 2009 Single dielectric barrier discharge plasma enhanced aerodynamics: physics, modeling and applications. *Exp. Fluids* **46**, 1–26.

DURBIN, P. & WU, X. 2007 Transition beneath vortical disturbances. *Annu. Rev. Fluid Mech.* **39**, 107–128.

HANSON, R. E., BADE, K. M., BELSON, B. A., NAGUIB, A. M., LAVOIE, P. & ROWLEY, C. W. 2014 Feedback control of slowly-varying transient growth by an array of plasma actuators. *Phys. Fluids* **26** (2), 024102.

HANSON, R. E., LAVOIE, P., BADE, K. M. & NAGUIB, A. M. 2012 Steady-state closed-loop control of bypass boundary layer transition using plasma actuators. *AIAA Paper* 2012-1140.

HANSON, R. E., LAVOIE, P., NAGUIB, A. M. & MORRISON, J. 2010 Transient growth instability cancellation by a plasma actuator array. *Exp. Fluids* **49**, 1339–1348.

JACOBSON, S. A. & REYNOLDS, W. C. 1998 Active control of streamwise vorticies and streaks in boundary layers. *J. Fluid Mech.* **360**, 179–211.

JUKES, T. N. & CHOI, K.-S. 2012 Dielectric-barrier-discharge vortex generators: characterisation and optimisation for flow separation control. *Exp. Fluids* **52**, 329–345.

JUKES, T. N. & CHOI, K.-S. 2013 On the formation of streamwise vortices by plasma vortex generators. *J. Fluid Mech.* **733**, 370–393.

LANDHAL, M. T. 1980 A note on an algebraic instability of inviscid parallel shear flows. *J. Fluid Mech.* **98**, 243–251.

LEMONIS, G. & DRACOS, T. 1995 A new calibration and data reduction method for turbulence measurement by multihotwire probes. *Exp. Fluids* **18**, 319–328.

LUNDELL, F. 2007 Reactive control of transition induced by free-stream turbulence: an experimental demonstration. *J. Fluid Mech.* **585**, 1–41.

LUNDELL, F., MONOKROUSES, A. & BRANDT, L. 2009 Feedback control of boundary layer bypass transition: experimental and numerical progress. *AIAA Paper* 2009-612.

MATSUBARA, M. & ALFREDSSON, P. H. 2001 Disturbance growth in boundary layers subjected to free-stream turbulence. *J. Fluid Mech.* **430**, 149–168.

NAGUIB, A. M., MARRISON, J. F. & ZAKI, T. A. 2010 On the relationship between the wall-shear-stress and transient-growth disturbances in a laminar boundary layer. *Phys. Fluids* **22** (5), 1–13.

NOLAN, K. P. & ZAKI, T. A. 2013 Conditional sampling of transitional boundary layers in pressure gradients. *J. Fluid Mech.* **728**, 306–339.

OSMOKROVIC, L. P., HANSON, R. E. & LAVOIE, P. 2015 Laminar boundary-layer response to spanwise periodic forcing by dielectric-barrier-discharge plasma-actuator arrays. *AIAA J.* **53** (3), 1–12.

PATTENDEN, R. J., TURNOCK, S. R. & ZHANG, X. 2005 Measurements of the flow over a low-aspect-ratio cylinder mounted on a ground plane. *Exp. Fluids* **39**, 10–21.

RESHOTKO, E. 2001 Transient growth: a factor in bypass transition. *Phys. Fluids* **13** (5), 1067–1075.

RIZZETTA, D. P. & VISBAL, M. R. 2007 Direct numerical simulations of flow past an array of distributed roughness elements. *AIAA J.* **45** (8), 1967–1976.

SARIC, W. S. 2007 Boundary-layer stability and transition. In *Springer Handbook of Experimental Fluid Mechanics* (ed. C. Tropea, A. L. Yarin & J. F. Foss), pp. 886–896. Springer.

SKOGESTAD, S. 2004 Simple analytic rules for model reduction and PID controller tuning. *Model. Ident. Control* **25** (2), 85–120.

VAUGHAN, N. J. & ZAKI, T. A. 2011 Stability of zero-pressure-gradient boundary layer distorted by unsteady Klebanoff streaks. *J. Fluid Mech.* **681**, 116–153.

VISBAL, M. R. 1991 The laminar horseshoe vortex system formed at a cylinder/plate juncture. In *22nd AIAA Fluid Dynamics, Plasma and Lasers Conference, Honolulu, HI, June 1–16*.

WHITE, E. B. 2002 Transient growth of stationary disturbances in a flat plate boundary layer. *Phys. Fluids* **14** (12), 4429–4439.

ZAKI, T. A. 2013 From streaks to spots and in to turbulence: exploring the dynamics of boundary layer transition. *Flow Turbul. Combust.* **91** (3), 451–473.

ZAKI, T. A. & DURBIN, P. A. 2005 Mode interaction and the bypass route to transition. *J. Fluid Mech.* **531**, 85–111.